Volume 46
DOE/DP40200-156

LLE Review

Quarterly Report

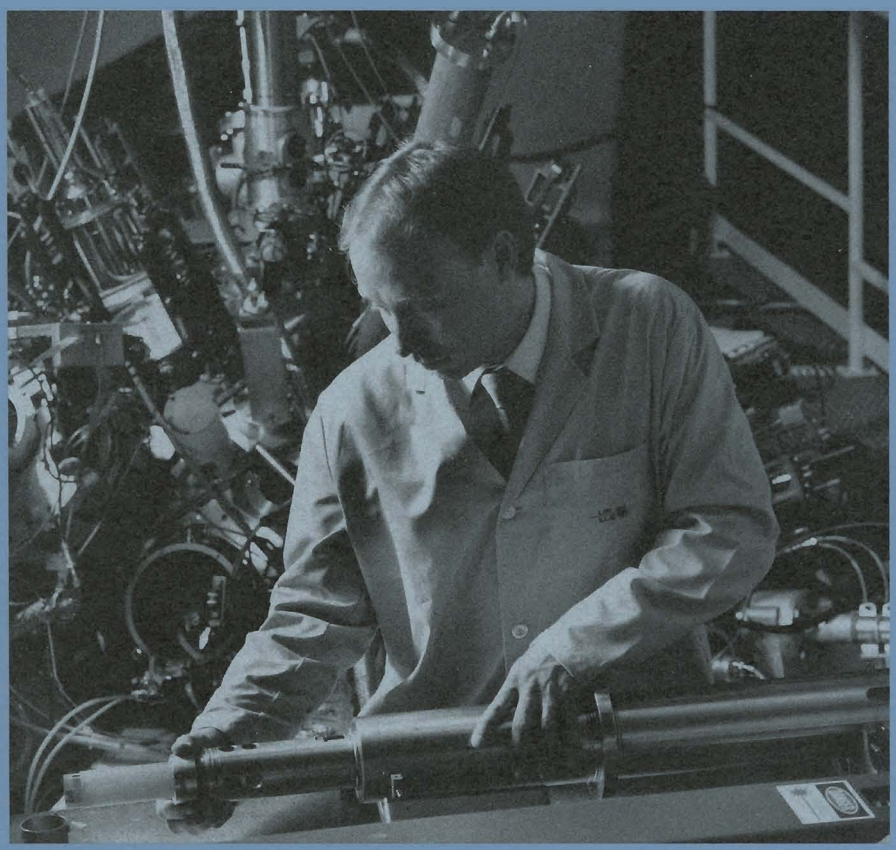

January–March 1991

Laboratory for Laser Energetics
College of Engineering and Applied Science
University of Rochester
250 East River Road
Rochester, New York 14623-1299

Volume 46
DOE/DP40200-156

LLE Review

Quarterly Report

Editor: E. M. Epperlein
(716) 275-8245

January–March 1991

Laboratory for Laser Energetics
College of Engineering and Applied Science
University of Rochester
250 East River Road
Rochester, New York 14623-1299

IN BRIEF

This volume of the LLE Review, covering the period January–March 1991, contains a report on how photoelectric fluorescence affects x-ray absorption lines in laser-plasma experiments, and a review of recent analysis of transverse instabilities of counterpropagating light waves in homogeneous plasmas.

The section on advanced technology has reports on the experimental characterization of Bessel beams, the design, testing, and use of a Kirkpatrick-Baez x-ray microscope on OMEGA, and the investigation of phase noise in mode-locked lasers.

The highlights of this issue are

- Investigation of the effect of photoelectric fluorescence on the formation of x-ray absorption lines has demonstrated that this process should not be neglected when analyzing experiments where the continuum is hardened by high core temperatures, opacity effects, or core components that radiate efficiently at ionizing energies.
- Properties of transverse instabilities driven by the ponderomotive force of light waves in homogeneous plasmas have been analyzed. It is shown that the convective instability of a single light wave can be transformed into an absolute instability in the presence of a second, counterpropagating light wave.

- It has been demonstrated experimentally that Bessel beams can be generated with intensity profiles that closely resemble the ideal J_o^2 transverse-intensity distribution. For applications where depth of focus and beam definition are of importance, Bessel beams present significant advantages over Gaussian beams.
- Kirkpatrick-Baez (KB) microscopes have been used on the OMEGA target chamber to image laser-plasma x rays for a number of years. Recently a testing facility for these microscopes has been assembled at LLE. This facility has been used to more fully characterize the resolution, field of view, and depth of field of these microscopes. A new KB microscope with gold-coated mirrors has been deployed on OMEGA enabling the imaging of higher-energy x rays (up to 7 keV).
- It has been found that thermal and acoustic effects can be significant sources of phase noise in short-pulse mode-locked lasers. Schemes for eliminating these problems have been discussed.

CONTENTS

Frederic Marshall, Research Scientist, is shown on the front cover assembling a Kirkpatrick-Baez x-ray microscope for installation on the OMEGA target chamber (background). Shown above is a closeup of the x-ray reflecting assembly (x-ray optics), which is described in the Advanced Technology Developments section of this issue of the LLE Review.

Section 1
PROGRESS IN LASER FUSION

1.A The Effect of Photoelectric Fluorescence on the Formation of X-Ray Absorption Lines in Laser-Plasma Experiments

In laser-plasma experiments, conditions in an embedded layer in a target shell can be inferred from the spectral attenuation of x-ray continuum radiation by the layer.[1] In such experiments, absorption lines are formed by 1s–2p absorption transitions in helium-like through fluorine-like species of certain ions in the layer to be diagnosed. The areal density of each species can be inferred from the attenuation in the spectrum within its respective band, provided the average 1s–2p absorption cross sections for each species are known and provided competing line-forming mechanisms are taken into account. In photoelectric fluorescence, which is one such potentially important competing mechanism, the formation of a 1s vacancy by photoionization is followed by 2p–1s spontaneous emission within the same spectral range as the 1s–2p absorption band of the same ion. The importance of photoelectric fluorescence depends on the supply of ionizing photons, which is sensitive to the design of the experiment. This process should be considered when analyzing experiments where the continuum is hardened by high core temperatures, by opacity effects, or by core components that radiate efficiently at ionizing energies.

Introduction

In absorption spectroscopy, absorption features impressed on the spectrum of a continuum background source are interpreted in terms of conditions in an absorbing foreground medium. If the opacity per ion caused by a particular transition beginning from some initial state is known, then

the areal density (i.e., the path integral of the density along the path of the continuum propagation) of ions in that state within the absorbing medium can be inferred from the attenuation of the background continuum caused by that transition.[2,3] If the relative abundance of ion species can be determined in this way, then temperature in the absorbing medium can also be inferred from the observed state of ionization, which can be modeled in terms of temperature and density.[3]

In x-ray spectra from inertial confinement fusion experiments and other laser-plasma experiments, the absorption features of interest are typically arrays of 1s–2p lines from the ground configuration and from certain low-lying excited configurations of L-shell ion species, fluorine-like through helium-like. The arrays from each species form a distinct band of absorption where the individual lines are usually not resolved. We consider here the contribution of photoelectric fluorescence to reducing the net attenuation of the continuum within each of these 1s–2p absorption bands.

Photoelectric fluorescence is the 2p–1s emission that follows the formation of a 1s vacancy by photoionization. These emission transitions are inverses of the transitions that form the absorption arrays, so fluorescence reduces the apparent line absorption. This emission is equivalent to the "K-alpha" emission lines caused by K-shell ionization as a result of the impact of suprathermal electrons[4] or photons[5] formed in the plasma corona of a target as it is illuminated by high-intensity infrared laser light.

The importance of photoelectric fluorescence will be estimated and expressed in terms of atomic parameters and local plasma conditions within a volume element by comparing local absorption and emission rates, rather than in the context of specific ions in a specific experimental geometry. In this way, the ranges of conditions and atomic parameters where photoelectric fluorescence has potential importance can be more easily recognized. Approximate formulae for atomic rates with explicit parameter dependences are used. The results show that typical continua from the cores of imploded targets can produce enough emission by photoelectric fluorescence to compete with absorption by photoexcitation and that quantitative interpretation of absorption spectra must take this effect into account.

In laser-driven, direct-drive inertial confinement experiments,[6] compression at the center of the target creates conditions of high density and temperature that produce a burst of continuum radiation near the time of peak compression. This radiation passes through the imploded shell of the target on its way to the spectrograph. This shell remnant usually remains within the range of temperatures where light elements in the neighborhood of chlorine (e.g., silicon through calcium) would be ionized to fluorine-like through helium-like states.[3] This temperature is typically of the order of a few hundred electron volts, which is much cooler than the temperatures in the coronal region and in the compressed core. Since these ions have partially vacant L shells, absorption lines can be imprinted on the passing background continuum by inner-shell absorption transitions of the kind 1s–2p. These

absorbing elements either occur naturally in the shell material itself, e.g., silicon in glass,[2] or they can be introduced as additives or deposited as a thin concentric layer inside the shell.[3]

Emission and Absorption

The probability that spontaneous emission will occur in an ion following the removal of a 1s electron is called the K-shell fluorescence efficiency ω_K.[7] In an isolated ion, Auger autoionization[8] is the other possible outcome, and ω_K is the branching ratio between Auger autoionization and spontaneous emission

$$\omega_K = \frac{A_{21}}{A_{21} + A_{\text{auto}}} , \tag{1}$$

where A_{21} and A_{auto} are the spontaneous emission and Auger autoionization rates, respectively.

The fraction of 1s vacancies formed by photoionization that lead to line emission is small, since $\omega_K << 1$ for low-Z species.[9] However, the supply of ionizing photons can be large enough, compared to the number of excitation photons within the 1s–2p absorption band, to yield a significant competing emission. The K-shell fluorescence efficiency also gives the probability of re-emission when a 1s vacancy is created by photoexcitation in the formation of absorption lines. This re-emission decreases the depth of the absorption lines, but the fraction of excitations that end in re-emission is generally neglected, again, since $\omega_K << 1$. Photoexcitation of higher transitions, such as 1s–3p, creates 1s vacancies that also decay, in part, via the 2p–1s radiative transitions, but this is a smaller effect and will be ignored here.

The fluorescence efficiencies generally quoted are values appropriate for isolated atoms or ions. In plasmas, electron collisional transitions from one autoionizing state to another can affect the fluorescence efficiency.[10] At higher densities ($n_e \sim 10^{24}$; see the following), the 1s vacancy can also be filled by radiative or collisional recombination or by collisional de-excitation,[11] and as these rates become comparable with spontaneous emission, fluorescence is quenched.

Rates and Approximations

The screened hydrogenic approximation is applicable to highly ionized species since spectator electrons have a smaller effect on electron orbits than the central nuclear charge, particularly for K-shell orbits that are largely internal to the spectator electrons and are thus least affected by them. This approximation is adequate for calculating a correction factor for the absorption. The explicit dependence of screened-hydrogenic rate expressions on atomic parameters is useful in expressing the importance of photoelectric fluorescence over a broad range of atomic parameters and local conditions.

Photoexcitation

The absorption cross section of a given transition i can be written in the form $\sigma_i \phi_i(\nu)$, where $\phi_i(\nu)$ is the line profile, normalized to unity with respect to integration over frequency ν, and where σ_i is the frequency-integrated cross section of the transition. The attenuated intensity $I(\nu)$ remaining after the incident background continuum intensity I_0 passes through a homogeneous layer of thickness Δr of material with a number density N_I of the absorbing species is

$$\ln\left[\frac{I_0}{I(\nu)}\right] = N_I \Delta r \, \sigma_i \phi_i(\nu) \ , \tag{2}$$

where

$$\sigma_i = \frac{\pi e^2}{m_e c} f \tag{3}$$

and f is the absorption oscillator strength of the transition.

In the simplest interpretation of this attenuation, neglecting instrumental broadening, foreground emission, etc., the areal density of the absorbing species $N_I \Delta r$ can be obtained from the integrated attenuation and from the integrated cross section σ_i, using

$$\int \ln\left[\frac{I_0}{I(\nu)}\right] d\nu = N_I \Delta r \sigma_i \ . \tag{4}$$

Note that this expression is independent of the line profile, which need not be considered further in this interpretation.[3]

The average absorption cross section for each species is obtained by averaging the cross sections of all 1s–2p transitions from all possible initial configurations, weighted according to the statistical weights of the initial states. The relevant species are helium-like through fluorine-like, and up to three initial configurations are possible, (1) $1s^2 2s^2 2p^n$ (ground), (2) $1s^2 2s 2p^{n+1}$ (singly excited), and (3) $1s^2 2p^{n+2}$ (doubly excited), subject to the restriction that there be no more than six 2p electrons in the final state. The average photoexcitation cross sections for each configuration used here are screened hydrogenic results scaled from the helium-like cross section σ_{He}, according to

$$\sigma_i = \sigma_{He}\left(1 - P_{2p}/6\right), \tag{5}$$

where P_{2p} is the occupation number of the 2p subshell. Even though the spectator charge in these ions varies from one to eight electrons (nearly half

the nuclear charge, in the case of argon), this approximation works very well, particularly for the relative absorption strengths of the configurations of a given species.[12]

The unresolved 1s–2p transition arrays from each contributing configuration coincide closely, so it suffices to treat them as a single feature with an effective absorption strength obtained by averaging over the three possible initial configurations. At typical shell temperatures, the low-lying $1s^2(2s+2p)^n$ configurations are linked by 2s–2p transitions that are readily excited by electron collisions. We assume, then, that these configurations are populated according to their statistical weights. At temperatures where these species will have non-negligible populations, this is a good approximation to the more correct weighting using the temperature-dependent Boltzmann ratio.[12,13]

The vacancy fractions and statistical weights for the L-shell configurations needed to evaluate Eq. (4) and to perform the appropriate configuration averaging are given in Table 46.I.

Photoionization

The photoionization rate is calculated in the screened hydrogenic approximation[14] assuming the Kramers cross section[15] per electron in principal level n

$$\sigma_{n,z}(\nu) = \frac{64\pi^4 e^{10} m_e z^4}{3\sqrt{3} h^6 c \nu^3 n^5} g_{PI}(z,n,\nu) , \tag{6}$$

with the Gaunt factor of Menzel and Pekeris[15]

$$g_{PI}(z,n,\nu) = 1 - 0.1728 \left(\frac{h\nu}{I_H z^2}\right)^{1/2} \left[\frac{2}{n^2}\left(\frac{I_H z^2}{h\nu}\right) - 1\right], \tag{7}$$

where I_H is the ground-state ionization energy of hydrogen, I_H = 13.6 eV.

Fluorescence Efficiency

Fluorescence efficiency for K-alpha emission from neutral atoms is well documented, theoretically and experimentally, but relatively little can be found on ionized atoms. We can infer fluorescence efficiencies for ions from the neutral values by the model of McGuire,[17] which compares well with Bhalla and Tunnell[18] for lithium-like argon and with McGuire for the L-shell ions of aluminum. In this model, the radiative decay probability of an ion with a K-shell vacancy $A_r P_{2p}$ is written to scale with P_{2p}, the number of 2p electrons, and the Auger ionization probability $A_a P_{2p}(P_{2p}-1)$ is written to scale with the number of pairs of 2p electrons. The latter product reflects the joint probability of one 2p electron decaying and transfering its energy to another 2p electron. The fluorescence efficiency, in terms of these rates, is

$$\omega_K = \frac{A_r P_{2p}}{A_r P_{2p} + A_a P_{2p}\left(P_{2p} - 1\right)} , \tag{8}$$

which is appropriate for isolated ions.

High-Density Effects on Fluorescence Efficiency

Fluorescence efficiency is usually derived for the case of an isolated ion, but local density of electrons can introduce additional processes that alter or quench it. It has been shown, for example, that electron collisions can rearrange the L-shell configuration of an ion quickly enough after the formation of a K-shell vacancy to affect the branching between autoionization and spontaneous emission.[10] Estimates of other corrections to the fluorescence efficiency of an isolated ion, given by Eq. (1), can be obtained by using the following approximate expressions for the processes of interest.

The rate of spontaneous emission from the $n = 2$ shell to the $n = 1$ shell is given by

$$A_{21} = 4.34 \times 10^7 \left(\sec^{-1}\right) f_{21} \left(\frac{\Delta E}{\mathrm{eV}}\right)^2 , \tag{9}$$

where ΔE is the transition energy, $f_{21} = 0.05125 \times P_2$ is the oscillator strength (based on the scaled hydrogenic result),[19] and P_2 is the number of L-shell electrons.

For collisional de-excitation[20]

$$C_{21} = 4.50 \times 10^{-6} \left(\sec^{-1}\right) \frac{n_e f_{21}}{\left(\frac{\Delta E}{\mathrm{eV}}\right)\left(\frac{T}{\mathrm{eV}}\right)^{1/2}} . \tag{10}$$

The rate coefficient α_3 for collisional 3-body recombination to level n of the species of charge Z to form the species of charge $Z-1$ is obtained from the detailed balance relationship

$$\alpha_3 = \frac{g_{Z-1}}{g_Z} \frac{n_e}{2} \left(\frac{h^2}{2\pi m_e kT}\right)^{3/2} e^{\chi_n / kT} S_n , \tag{11a}$$

where g_Z and g_{Z-1} are the respective statistical weights of the relevant species, and from S_n, the rate coefficient of collisional ionization from level n[21]

$$S_n = 3.0 \times 10^{-6} \left(\sec^{-1}\right) \frac{\left(\frac{n_e}{\mathrm{cm}^{-3}}\right) P_n Ei\left(\frac{\chi_n}{T}\right)}{\left(\frac{T}{\mathrm{eV}}\right)^{3/2} \left(\frac{\chi_n}{T}\right)} . \tag{11b}$$

The exponential integral $Ei(x)$ is given by the rational approximation

$$e^x Ei(x) \cong \frac{1.25}{1.00+1.25x} . \tag{11c}$$

The rate coefficient of K-shell radiative recombination is given by[22]

$$\alpha_r = 5.20\times10^{-14}\left(\sec^{-1}\right)\left(\frac{n_e}{\mathrm{cm}^{-3}}\right)Z\left(1-\frac{P_{1s}}{2}\right)\left(\frac{\chi}{T}\right)^{3/2} e^{\chi/T}Ei\left(\frac{\chi}{T}\right) . \tag{12}$$

The rate coefficients in Eqs. (9)–(12) are written with the electron density n_e in electrons per cubic centimeter, and with the ionization energies χ, the excitation energy ΔE, and the electron temperature T all in electron volts. With these expressions, a corrected fluorescence efficiency can be written that includes the effects of radiative and collisional recombination and collisional de-excitation,

$$\omega_K^* = \frac{\omega_K}{1+(C_{21}+\alpha_3+\alpha_r)(\omega_K/A_{21})} , \tag{13}$$

where

$$\frac{\omega_K C_{21}}{A_{21}} = 9.60\times10^{-2}\frac{\left(\frac{\omega_K}{0.25}\right)\left(\frac{n_e}{10^{24}\,\mathrm{cm}^{-3}}\right)}{\left(\frac{h\nu_0}{3\ \mathrm{keV}}\right)^3\left(\frac{T}{100\ \mathrm{eV}}\right)^{1/2}} , \tag{14}$$

$$\frac{\omega_K \alpha_3}{A_{21}} = 3.88\times10^{-3}\frac{\left(\frac{\omega_K}{0.25}\right)\left(\frac{n_e}{10^{24}\,\mathrm{cm}^{-3}}\right)^2}{\left(\frac{h\nu_0}{3\ \mathrm{keV}}\right)^4\left(\frac{T}{100\ \mathrm{eV}}\right)P_2} , \tag{15}$$

and

$$\frac{\omega_K \alpha_r}{A_{21}} = 0.0344\frac{\left(\frac{\omega_K}{0.25}\right)\left(\frac{n_e}{10^{24}\,\mathrm{cm}^{-3}}\right)\left(\frac{Z}{16}\right)}{\left(\frac{h\nu_0}{3\ \mathrm{keV}}\right)^{3/2}\left(\frac{T}{100\ \mathrm{eV}}\right)^{1/2}P_2} \tag{16}$$

These correction terms are expressed in terms of scaling parameters normalized to values appropriate for argon at a nominal temperature of 200 eV and a nominal electron density of $10^{24}\,\mathrm{cm}^{-3}$. Under these conditions, the correction to the fluorescence efficiency is small. Should the shell reach significantly higher densities, fluorescence could actually be quenched, thus greatly simplifying the task of including it in a model of the absorption signal. These preliminary results show that careful modeling of all the processes that contribute to the fluorescence efficiency can be important to the modeling of the 1s–2p absorption signal.

Table 46.I: Average parameters for the configurations of chlorine ions.

Configuration	Weighted Oscillator Strength (gf)	Statistical Weight	2p Vacancy	Species Average 2p Vacancy	Average gf Per Unit Vacancy
Helium-like					
$1s^2$	0.882	1	6	6.00	0.822
Lithium-like					
$1s^22s$	1.559	2	6	5.25	0.788
$1s^22p$	3.864	6	5		
Beryllium-like					
$1s^22s^2$	0.745	1	6	4.50	0.780
$1s^22s2p$	7.594	12	5		
$1s^22p^2$	7.484	15	4		
Boron-like					
$1s^22s^22p$	3.657	6	5	3.75	0.770
$1s^22s2p^2$	14.705	30	4		
$1s^22p^3$	7.262	20	3		
Carbon-like					
$1s^22s^22p^2$	7.09	15	4	3.00	0.759
$1s^22s2p^3$	14.230	40	3		
$1s^22p^4$	3.500	15	2		
Nitrogen-like					
$1s^22s^22p^3$	6.867	20	3	2.25	0.747
$1s^22s2p^4$	6.867	30	2		
$1s^22p^5$	0.676	6	1		
Oxygen-like					
$1s^22s^22p^4$	3.288	15	2	1.50	0.723
$1s^22s2p^5$	1.317	12	1		
$1s^22p^6$	0.0	1	0		
Fluorine-like					
$1s^22s^22p^5$	0.635	6	1	0.75	0.707
$1s^22s2p^6$	0.0	2	0		

TC2968

Results and Discussions

The effect of interest is the filling of absorption lines by fluorescence emission. A measure of the importance of the photoelectric fluorescence effect, relative to photoexcitation, can be expressed in terms of the local rates of emission and absorption, which are functions of local plasma conditions. One such measure is the number of fluorescent photons emitted for each photon absorbed and destroyed within the 1s–2p transition band of a given ion species

$$\left(\frac{\text{fluorescence}}{\text{absorption}}\right) = \frac{\omega_K N_{Z-1} \int_{\chi_0/h}^{\infty} \frac{I(\nu)}{h\nu} \sigma_{K,Z-1}(\nu) d\nu}{(1-\omega_K) N_Z \frac{I(\nu_0)}{h\nu_0} \sigma_{i,z}} \quad . \tag{17}$$

The K-shell photoionization rate is determined by the cross section $\sigma_{K,Z-1}$ for the removal of a K-shell electron from the species of charge $Z-1$ due to photons above the ionization energy χ_{Z-1}. The form of the local radiation continuum $I(\nu)$ and the relative populations of ions of the absorbing species N_Z and ions of the photoionization parent species N_{Z-1} must be specified. The species of charge $Z-1$ is photoionized into excited states of the absorbing species of charge Z that subsequently radiate into the absorption band, in direct competition with the formation of the absorption line. The $(1-\omega_K)$ factor multiplying the photoexcitation rate in the denominator represents a correction for re-emission.

The continuum is characterized by a temperature T and by an index q that spans spectra from a free-free continuum ($q = 0$) to the high-energy Wien limit of a blackbody ($q = 3$)

$$I(\nu) \sim \nu^q e^{-\tau_0 (\nu_0/\nu)^3} e^{-h\nu/kT} \quad . \tag{18}$$

An attenuation factor is included that represents the modification of the continuum due to a bound-free absorbing layer. The optical depth of this absorber is τ_0 at line center and extrapolates to lower opacity at higher energies where photoionization takes place, thus hardening the continuum and enhancing fluorescence relative to photoexcitation.

In Fig. 46.1, the ratio $F(T, q, \tau_0)$ of the number of photoelectric fluorescence photons emitted to the number of photoexcitation photons absorbed within the total 1s–2p transition signal of the boron-like species of argon is plotted as a function of the continuum temperature for various continua, assuming equal numbers of boron-like and carbon-like ions. The fluorescence filling ratio scales to other ions as

$$\left(\frac{\text{fluorescence}}{\text{absorption}}\right) \cong F(T,q,\tau_0) \frac{N_{Z-1}}{N_Z} \frac{\left(\frac{\omega_k}{0.25}\right)}{\left(\frac{1-\omega_k}{0.75}\right)\left(\frac{1-P_{2p}/6}{0.5}\right)} \quad . \tag{19}$$

The nominal $\omega_K = 0.25$ value for boron-like argon is estimated based on the value $\omega_K = 0.127$ for neutral argon[23] and the scaling suggested by Eq. (8). The set of solid curves is obtained from exponential continua typical of optically thin emission $q = 0$, and the dashed curves represent the high-energy Wien limit of the blackbody spectrum $q = 3$. Each curve within each set has been calculated for various values of the preabsorber optical depth ($\tau_0 = 0, 1, 2,$ and 3) at the line center. Absorbing layers of any optical depth can be considered, but beyond some point, the attenuation will make the absorption signal too small to be useful.

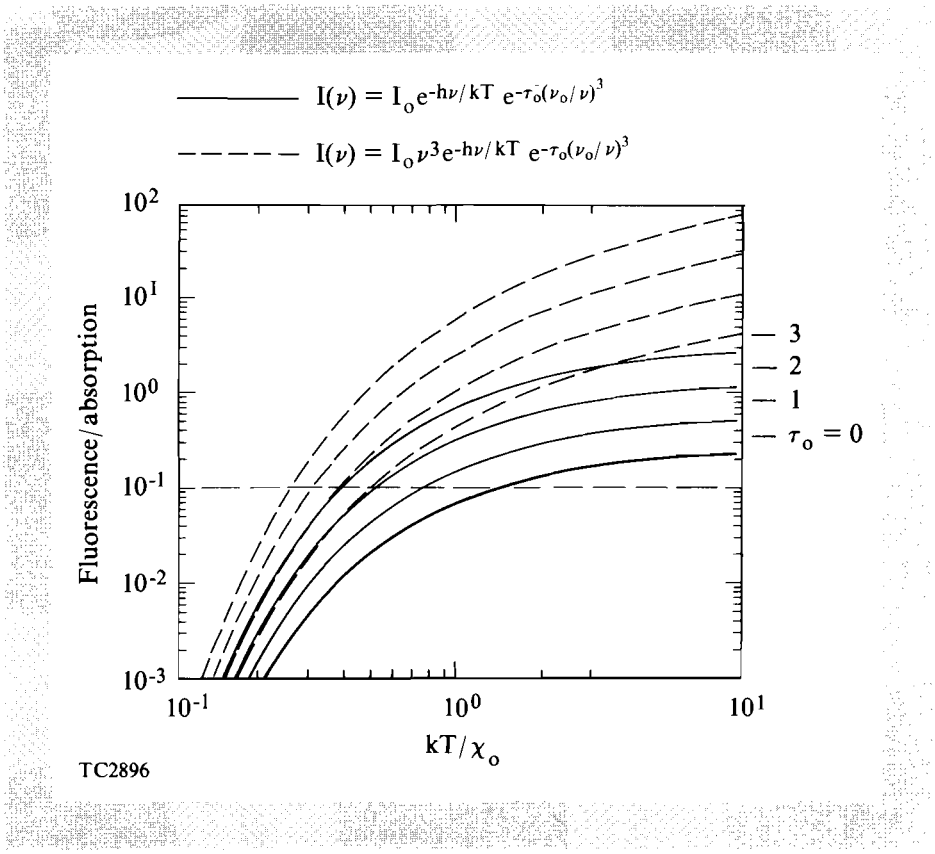

Fig. 46.1
The ratio of the number of photoelectric fluorescence photons emitted to the number of photoexcitation photons absorbed within the total 1s–2p transition band of the boron-like species of argon is plotted as a function of the continuum temperature for various continuum spectra. It is assumed that equal numbers of boron-like and carbon-like ions are present. The set of solid curves is obtained from exponential continua typical of optically thin emission, and the set of dashed curves represents the high-energy Wien limit of the blackbody spectrum. Each curve within the two sets has been calculated assuming that the continuum is filtered by a bound-free or free-free absorbing of optical depth τ_0 (0, 1, 2, and 3) at the line center. The marks by the right-hand axis give the high-temperature limit of the optically thin results.

Figure 46.1 shows that fluorescence can have an effect of 10% or more on the net absorption signal over a broad range of parameters, so it should be included in calculations involving absorption-line formation. It is also seen that fluorescent emission can fill the absorption lines only for continuum temperatures much higher than the ionization energy and/or for strong continuum hardening by an absorber. Hardening will be especially prominent for highly compressed targets having a high-Z absorbing layer, where the opacity is higher. Opacity will also be higher in lower-Z materials, such as carbon, if the absorbing layer is cool enough for bound-free-absorbing species to be abundant.

A special case arises when a high-Z fill gas, such as argon, is compressed with a radial temperature gradient. The central core can give rise to a strong continuum that produces absorption lines in the cooler, peripheral layer of the fill gas. The jump in the emission spectrum above the K-edge of, say, the helium-like ions will be efficient in producing photoionization in the peripheral layer. However, the absorption lines are located below the K-edge, where the continuum intensity is lower, which results in enhanced photoionization, relative to photoexcitation, as compared with the case of a smoother continuum spectrum.

Caution should be exercised in applying these results in the following instances: (a) The observation of K-alpha lines in emission need not be

interpreted as evidence of overwhelming fluorescence. This is because the continuum emitted by the outer, laser-heated target layer (especially if it is a high-Z layer) can excite K-alpha lines while propagating inwards. This could result in observable K-alpha emission lines without contributing to observable absorption lines. Figure 46.1 shows that local fluorescence-absorption ratios near and above unity are unlikely. For thin ($q = 0$) continua, this requires high temperatures ($kT > \chi_0$) and enough opacity hardening to obscure the signal substantially ($\tau_0 > 3$). (b) The comparison of local emission and absorption rates as an indication of the relative importance of fluorescence and absorption, i.e., the ratio given by Eq. (17), applies only to a representative sample of all the radiation escaping the plasma and may not conform to the measurements when, for example, the recorded spectrum is spatially resolved, especially if the continuum is emitted by a small, compressed core. The emission along the line of sight that traverses the center of the target under-represents the fluorescence. On the other hand, a line of sight that does not traverse the center may partly miss the absorption lines, but not the fluorescence emission. (c) The previously calculated ratio of fluorescence and absorption is valid when the absorption is weak enough not to reach saturation (i.e., depletion of the incident continuum photons). Since photoexcitation is a resonance effect, it will reach saturation before photoionization does. However, by the time saturation is reached, the absorption lines start to lose their diagnostic value and can at best be used to obtain a lower bound on the shell $\rho\Delta r$.

In deriving Eq. (17), it is assumed that the fluorescence spectrum is determined by the population distribution of L-shell ion species, the rate at which K-shell ionization and excitation produces K-shell vacancies in these ions, and the rate at which these vacancies decay. This requires the assumption that the K-shell fluorescence processes occur rapidly, before the ionization state of the newly formed [1s] ions, those with K-shell vacancies (e.g., $1s2s^n2p^m$), can redistribute. Such changes would alter the fluorescence spectrum. The distribution of L-shell configurations of the [1s] ions will evolve at a rate corresponding to the net difference in L-shell ionization and recombination rates. This net rate is proportional to the degree to which the [1s] ions are out of ionization equilibrium and is likely to be much less than the individual rates. In particular, the initial distribution of [1s] ions formed by ionization will be close to equilibrium because the parent $1s^2$ ions (e.g., $1s^22s^n2p^m$) would most likely be close to equilibrium and because the K-shell ionization rates change relatively little from species to species. The distribution of [1s] species formed by photoexcitation, on the other hand, could be skewed because the relevant cross sections are proportional to the L-shell vacancy fractions of the parent ions. What is likely to cause the distribution of [1s] species to relax before fluorescence could occur is, for example, L-shell radiative recombination, which determines the plasma ionization state over a wide range of conditions. At the same time, however, K-shell radiative recombination would quench the fluorescence at a comparable rate. A preliminary assessment, then, is that the fluorescence spectrum should not be altered by L-shell effects, except under circumstances that would quench the fluorescence altogether.

Conclusions and Summary

It is difficult to accurately predict the importance of an effect such as photoelectric fluorescence in a given experiment without full simulations. Nevertheless, the parameter dependences and scaling behaviors revealed in the simple calculation in this article should serve as a useful guide to anyone asking whether or not this effect is relevant to a particular experiment or simulation.

Even though other effects, such as inhomogeneities in temperature and density and the nonuniform sampling of the shell by a compact continuum source, can introduce comparable uncertainties and ambiguities into estimates of areal densities, the effect of the photoelectric fluorescence is systematic and should not be neglected.

ACKNOWLEDGMENT

This work was supported by the U.S. Department of Energy Division of Inertial Fusion under agreement No. DE-FC03-85DP40200 and by the Laser Fusion Feasibility Project at the Laboratory for Laser Energetics, which has the following sponsors: Empire State Electric Energy Research Corporation, New York State Energy Research and Development Authority, Ontario Hydro, and the University of Rochester.

REFERENCES

1. B. Yaakobi, R. L. McCrory, S. Skupsky, J. A. Delettrez, P. Bourke, H. Deckman, C. F. Hooper, and J. M. Soures, *Opt. Commun.* **34**, 213 (1980).
2. *Ibid.*; A. Hauer, in *Spectral Line Shapes,* edited by B. Wende (W. de Gruyter & Co., Berlin, 1981); D. K. Bradley, J. D. Hares, and J. D. Kilkenny, Rutherford-Appleton Laboratory, Annual Report No. RL-83-043, 1983, p. 5.4.
3. A. Hauer, R. D. Cowan, B. Yaakobi, O. Barnouin, and R. Epstein, *Phys. Rev. A* **34**, 411 (1986).
4. B. Yaakobi, I. Pelah, and J. Hoose, *Phys. Rev. Lett.* **37**, 836 (1976).
5. J. D. Hares, J. D. Kilkenny, M. H. Key, and J. G. Lunney, *Phys. Rev. Lett.* **42**, 1216 (1979); A. Hauer, W. Priedhorsky, and D. van Hulsteyn, *Appl. Opt.* **20**, 3477 (1981); and B. Yaakobi, J. A. Delettrez, L. M. Goldman, R. L. McCrory, W. Seka, and J. M. Soures, *Opt. Commun.* **41**, 355 (1982).
6. R. S. Craxton, R. L. McCrory, and J. M. Soures, *Sci. Am.* **255**, 68 (1986).
7. E. J. McGuire, in *Atomic Inner-Shell Processes*, edited by B. Crasemann (Academic Press, New York, 1975), Vol. I, pp. 293–330.
8. P. Auger, *J. Phys. Radium* **6**, 205 (1925).
9. H. U. Freund, *X-Ray Spectrometry* **4**, 90 (1975).
10. V. L. Jacobs and J. Davis, *Phys. Rev. A* **18**, 697 (1978).
11. D. Duston, J. E. Rogerson, J. Davis, and M. Blaha, *Phys. Rev. A* **28**, 2968 (1983).
12. R. Epstein, *Phys. Rev. A* **43**, 961 (1991).

13. LLE Rev. **24**, 169 (1985); C. Fievet, Thèse de Doctorat, Paris XI University, Orsay, France, 1989, quoted in C. Chenais-Popovics *et al.*, *Phys. Rev. A* **40**, 3194 (1989).

14. H. A. Bethe and E. E. Salpeter, *Quantum Mechanics of One- and Two-Electron Atoms* (Plenum, New York, 1977), pp. 297, 305, 316.

15. H. A. Kramers, *Philos. Mag.* **46**, 836 (1923); J. A. Gaunt, *Philos. Trans. R. Soc. London A* **229**, 163 (1930).

16. D. H. Menzel and C. L. Pekeris, *Mon. Not. Roy. Astron. Soc.* **96**, 77 (1935).

17. E. J. McGuire, *Phys. Rev.* **185**, 1 (1969).

18. C. P. Bhalla and T. W. Tunnell, *J. Quant. Spectrosc. Radiat. & Transfer* **32**, 141 (1984).

19. H. A. Bethe and E. E. Salpeter, *ibid.*, pp. 251, 266.

20. H. R. Griem, *Plasma Spectroscopy* (McGraw-Hill, New York, 1964), p. 147.

21. W. Lotz, *Z. Phys.* **216**, 241 (1968), quoted in D. Salzmann and A. Krumbein, *J. Appl. Phys.* **49**, 3229 (1978).

22. H. R. Griem, *ibid.*, p. 112, quoted in R. Epstein, S. Skupsky, and J. Delettrez, *J. Quant. Spectrosc. Radiat. & Transfer* **35**, 131 (1986).

23. E. J. McGuire, *Phys. Rev. A* **2**, 273 (1970).

1.B Transverse Instabilities of Counterpropagating Light Waves

Instabilities of Counterpropagating Waves in ICF

Direct-drive laser fusion requires high-gain fusion pellets to overcome the inherent losses associated with initiating the inertial fusion process. Conversion of laser light into energy used to drive the compression of the fuel pellet begins in the corona where the intense laser field must penetrate a plasma and deposit its energy into the pellet material. Two critical aspects of this deposition process are (1) the laser absorption efficiency and (2) the implosion symmetry.[1,2]

In the direct-drive fusion process both absorption efficiency and implosion symmetry can be adversely affected by parametric and focusing instabilities that occur during the interaction of the laser light with the coronal plasma. Focusing instabilities can degrade the uniformity of the laser light as it passes through the corona by enhancing modulations of the laser profile and distributing the incident laser light into filaments. This nonuniform deposition of laser energy can seed hydrodynamic instabilities that further degrade the laser-to-fuel coupling efficiency and inhibit the fusion gain.

Parametric instabilities can degrade the absorption of laser light by scattering it away from the pellet. More importantly, they are one source of hot electrons that can divert energy from the ablation process and preheat the fuel.

In this article, we discuss parametric and focusing instabilities arising because of the coupling of laser light to ion modes.[3,4] Though recent studies have shown that shorter-wavelength lasers[5] significantly reduce the effect of these instabilities, there is still much to be learned about their role in reactor-size plasmas. In addition to being important in ICF, these instabilities play a fundamental role in the interaction of laser light with other nonlinear optical materials and are of general interest.

Parametric and focusing instabilities need not occur in isolation. In fact, Brillouin scattering and filamentation are known to be closely related,[3,4] and recent studies have shown a correlation between the generation of Brillouin-scattered light and Raman-scattered light.[6–8] This article contains a description of a preliminary study of the transverse modulational instability in a plasma with adiabatic ion response when feedback from a counterpropagating wave is present. Several researchers have studied the effects of back-scattered or back-reflected light on parametric instabilities in laser-produced plasmas.[9–11] The backward propagating light may arise because of reflection of the incident laser from the critical surface, parametric back-scattering, or shinethrough, as shown in Fig. 46.2. In related applications, such as optical phase conjugation and x-ray lasers, the counterpropagating laser field is externally applied.

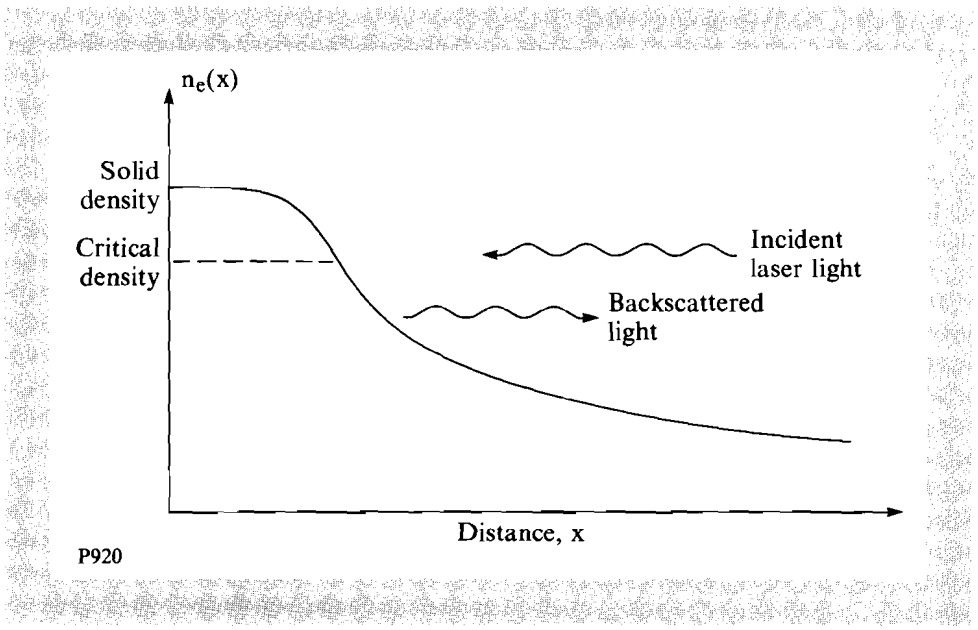

Fig. 46.2
Feedback from light propagating back towards the incident laser can arise from several sources.

Studies on the effect of counterpropagating laser fields in plasmas are closely related to basic nonlinear optics research in which the effect of a counterpropagating laser beam on parametric scattering and four-wave mixing has been investigated.[12,13] In addition, researchers in nonlinear optics have investigated the effect of a counterpropagating laser beam on transverse modulational instabilities in nonresonant media.[14–20] This work on nonresonant transverse modulational instabilities has been extended to include the resonant effects of the ion-acoustic response of a plasma. Though the model discussed here is simplified with respect to laser-plasma interactions, it is expected to be of direct relevance to the study of basic physics in, and applications of, nonlinear optical systems. In addition, this work provides a solid starting point for further laser-plasma interaction research.

Four-Sideband Instabilities

In this section the dominant interactions in the counterpropagating-wave system are introduced. A pair of intense, counterpropagating light waves, of frequency ω_0 and wave vector $\pm\boldsymbol{k}_0$, irradiate opposite ends of a homogeneous plasma of length L. Let $\boldsymbol{F}_0$ be the amplitude of the intense pump wave injected at the left end of the plasma, while $\boldsymbol{B}_0$ is the amplitude injected from the right end of the plasma. At high intensity, the ions respond to the presence of the light fields. Thus, since the index of refraction of the plasma is a function of the plasma density, it responds to the intensity of the fields on the ion-acoustic time scale.

Small-amplitude sidebands of the intense counterpropagating light waves can arise in the system as a result of noise within the plasma or by injection from an external source. Consider a single, small-amplitude, anti-Stokes sideband $\mathbf{F}_+$, which has frequency $\omega_0 + \omega$ and wave vector $\boldsymbol{k}_0 + \boldsymbol{k}$ as shown in Fig. 46.3. This sideband can interfere with the pump fields, creating periodic variations in the intensity that drive a grating in the index of refraction. In a plasma, these gratings can be driven at the frequency and wave number of the ion-acoustic wave. Since the ion-acoustic wave is a natural mode of the plasma, the gratings can be driven resonantly. Once a grating is formed, the pump fields can scatter from it to augment the sidebands.

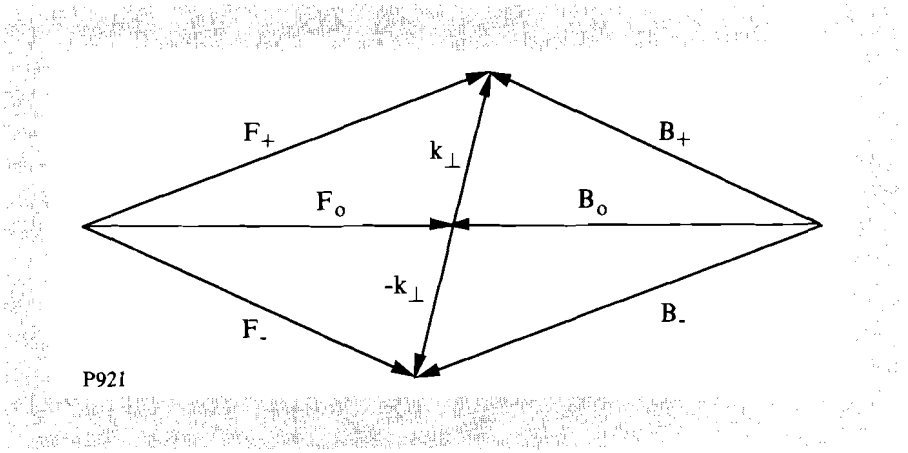

Fig. 46.3
The wave-vector matching diagram for the four-sideband interaction.

One distinct set of sidebands grows more strongly than the others. The phases of these modes are tuned in such a way that their linear and nonlinear phase shifts are optimally matched inside the medium. As a result, these optimally phase-matched modes exchange energy with the pump fields more efficiently than the unmatched modes can. In many instances these phase-matched sidebands are unstable. The counterpropagating-wave interaction can support two types of instabilities. At moderate intensity sidebands can grow as they propagate and are said to be convectively unstable. At higher intensity unstable sidebands can grow exponentially in time at each point in the plasma. This latter form of instability is called an absolute instability and grows in the frame of the medium without convecting away.

In the counterpropagating-wave system the two pump waves interact most strongly with a set of four sidebands that lie in a plane that includes the pump axis. Thus, the $\boldsymbol{F}_+$ sideband couples most strongly to the three other sidebands shown in Fig. 46.3. It couples with the Stokes-shifted sideband $\boldsymbol{F}_-$ as a result of a forward four-wave mixing process. It couples with the anti-Stokes sideband $\boldsymbol{B}_+$ as a result of Bragg reflection, and it couples with the Stokes-shifted sideband $\boldsymbol{B}_-$ as a result of a backward four-wave mixing process. In this article the linear stability of the four-sideband interaction is of primary interest, so let $|\boldsymbol{F}_0|, |\boldsymbol{B}_0| \gg |\boldsymbol{F}_\pm|, |\boldsymbol{B}_\pm|$. This system is expected to be coupled most strongly when the sidebands are polarized parallel to one another and to the pump waves, so let each wave be linearly polarized parallel to each of the other waves.

Growth of the four sidebands can occur as a result of several different fundamental interactions. The pure four-sideband interaction results from the concurrent interaction of all four sidebands with the pumps and occurs when the two oppositely propagating pump fields and the four sidebands are all simultaneously phase matched. This interaction is a true four-sideband resonance. As this four-sideband resonance is detuned, four two-sideband interactions are recovered.

The two-sideband forward four-wave mixing process occurs when a single pump field couples to a Stokes and an anti-Stokes sideband. Both sidebands propagate in the same direction as the pump field, but each sideband has a small perpendicular wave-number component. Thus, the $\boldsymbol{F}_+$ sideband couples with the pump $\boldsymbol{F}_0$ to drive a grating at $(\omega,\boldsymbol{k}_\perp)$. The $\boldsymbol{F}_0$ pump then scatters off of this grating to create the $\boldsymbol{F}_-$ sideband as shown in Fig. 46.4(a). Note that in general the wave-vector shift of the sideband need not be small and perpendicular with respect to the pump wave vectors. However, since the most important near-axis scattering processes obey this restriction, the more general cases are neglected for the purposes of this article.

Taken together, this pair of sidebands is equivalent to a transverse spatial modulation of the light-wave intensity profile. Since the index of refraction increases with increased intensity, a positive feedback loop is created between the field intensity and the medium. As a result, these transverse modulations grow as the interaction proceeds. This near-forward scattering

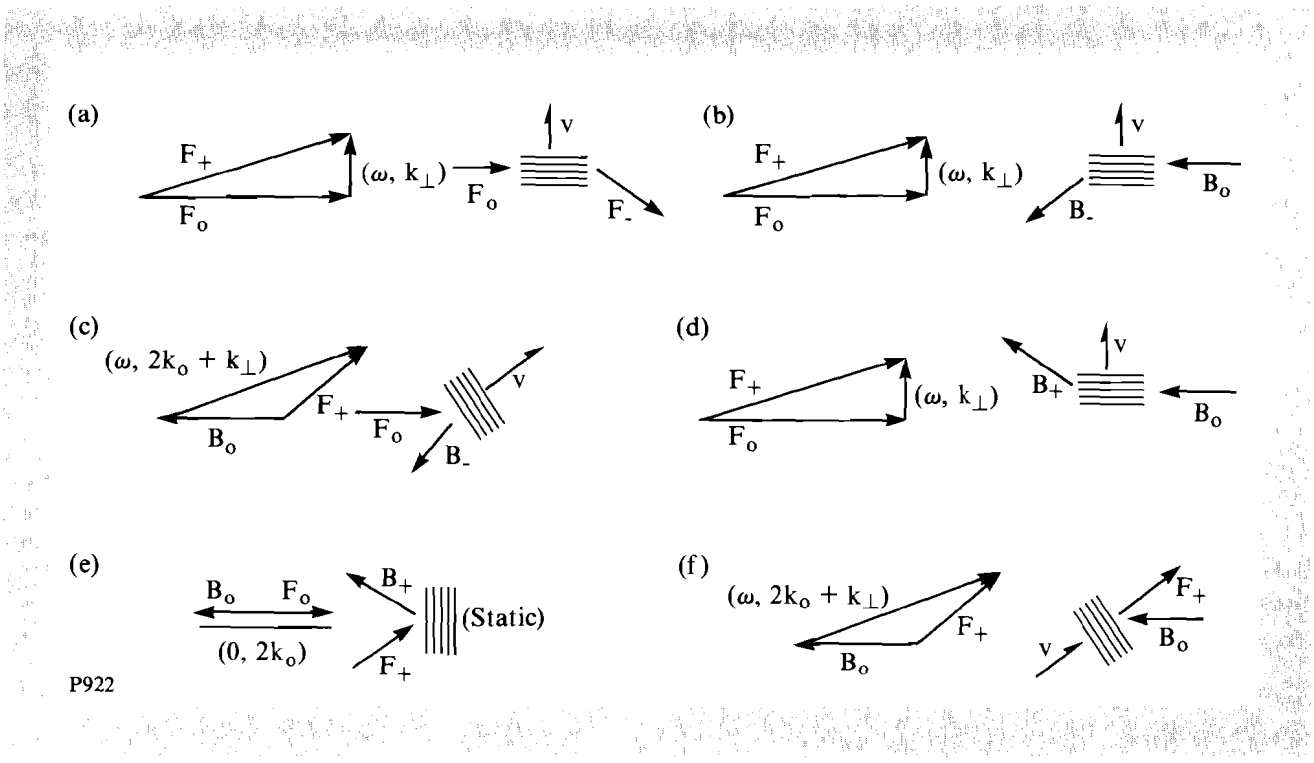

Fig. 46.4
Each two-sideband interaction is shown. (a) Forward four-wave mixing from the short wave-number grating, (b) backward four-wave mixing, (c) backward four-wave mixing from the static $2k_0$ grating, (d) backward phase conjugation from the short-wavelength grating, (e) backward phase conjugation from the long-wavelength grating, and (f) forward four-wave mixing from the large wave-number grating.

instability is the transverse modulational instability, and is associated with filamentation and self-focusing in its fully nonlinear manifestation. The transverse modulational instability has a dominant band of unstable transverse perturbation wave numbers. As a result, the transverse spatial Fourier spectrum of the scattered light will contain sidebands centered on the optimal transverse perturbation wave number or equivalently at the optimal cone angle. These sidebands are a signature of the instability. Thus, the transverse modulational instability can be thought of as self-induced diffraction. Since this interaction is invariant to rotations about the collinear pump axis, a probe sideband injected at any point on the circle determined by the cone angle will result in the appearance of a signal sideband located exactly opposite the probe on the same circle. When this convective instability is seeded by noise, all orientations of the sidebands are seeded equally and conical emission occurs.

Two different two-sideband backward four-wave mixing processes can also occur. Phase conjugate backward four-wave mixing occurs when a pair of oppositely propagating pump fields couple to a Stokes and anti-Stokes sideband that propagate exactly opposite to each other as shown in Figs. 46.4(b) and 46.4(c). This phase-conjugate coupling has been studied extensively in the past. Recall that as the intensity of the pump fields is increased, the phase-conjugate interaction becomes absolutely unstable. A less important backward four-wave mixing process occurs when a pair of oppositely propagating pump fields couple to a pair of oppositely propagating Stokes or anti-Stokes sidebands as shown in Figs. 46.4(d) and 46.4(e). This process corresponds to Bragg reflection.

Finally, a Stokes or anti-Stokes sideband can couple to the oppositely propagating pump to drive a short-wavelength grating as shown in Fig. 46.4(f). The same pump that drives the grating can scatter from the grating to enhance the sideband with which it is coupled. Note that either the Stokes or anti-Stokes sideband can couple with the oppositely propagating pump field. This interaction is stimulated Brillouin scattering and requires the ion-acoustic grating to be driven resonantly. In a plasma each of the two sideband interactions is enhanced near the ion-acoustic resonance. Resonantly enhanced four-wave mixing and phase conjugation in plasmas is of great current interest.[21] In addition, some researchers have begun to investigate resonant self-focusing in plasmas.[22]

Origin of the Four-Sideband Equations

In this section the origin of the governing equations for the four-sideband interaction is discussed. A model describing the coupling of the transverse electromagnetic fields of two light waves propagating in a quasi-neutral plasma can be developed with Maxwell's equations when they are coupled to the two-fluid equations of motion for the plasma. The fluid equations take the form

$$\partial_t n_s + \nabla \cdot (n_s \boldsymbol{V}_s) = 0,$$

$$\partial_t \boldsymbol{V}_s + (\boldsymbol{V}_s \cdot \nabla)\boldsymbol{V}_s = -\nabla P_s / n_s m_s + q_s(\boldsymbol{E} + \boldsymbol{V}_s \times \boldsymbol{B}/c)/m_s,$$

where the subscript s denotes the particle species (electron or ion). $\boldsymbol{V}_s$ is the velocity field of one plasma species, P_s is the pressure, and q_s is the particle charge. The charge and current densities that drive Maxwell's equations are

$$\rho = \sum_s n_s q_s, \quad \boldsymbol{J} = \sum_s n_s q_s \boldsymbol{V}_s,$$

respectively. In equilibrium, $n_e(0) = Zn_i(0) = n_0$, where Z is the ionization number and $\boldsymbol{V}_e(0) = \boldsymbol{V}_i(0) = 0$. It can be seen from the momentum equation that the first-order electron motion is in the direction of the applied electric field. Thus

$$\boldsymbol{V}_\perp = e\boldsymbol{A}_\perp / m_e c,$$

where $\boldsymbol{A}_\perp$ is the transverse component of the vector potential. Assuming that the low-frequency plasma evolution is quasi-neutral, then $n_e^{(1)} \approx Zn_i^{(1)}$, and the following set of equations governing the evolution of $\boldsymbol{V}_\perp$ and $\langle n \rangle = n_e^{(1)}/n_0$ arises from the root equations

$$\left[\partial_{tt} + \omega_e^2 - c^2\nabla^2\right]\boldsymbol{V}_\perp = -\omega_e^2 \langle n \rangle \boldsymbol{V}_\perp$$

$$\left[\partial_{tt} - 2i\gamma\partial_t - c_s^2\nabla^2\right]\langle n \rangle = Ze^2\nabla^2\left\langle \boldsymbol{V}_\perp^2 \right\rangle / 2c^2 m_e m_i,$$

where $\langle\ \rangle$ denotes an average over the high-frequency components, $c_s^2 = Z T_e^{(0)}/m_i$ is the ion-sound speed, and $T_e^{(0)}$ is the equilibrium electron

temperature. The first equation is the analog of Maxwell's wave equation for the electric field driven by the time derivative of the material polarization. The second equation is the sound-wave equation driven by the low-frequency variations in light pressure.

The dependent variable $\boldsymbol{V}_\perp$ varies on the fast time scale of the electromagnetic fields and on the slow time scale of the ions. This variable represents the total field and can be written

$$\boldsymbol{V}_\perp = (1/2)(\boldsymbol{F}_0 + \boldsymbol{F}_+ + \boldsymbol{F}_-)\exp[i(\boldsymbol{k}_0 \cdot \boldsymbol{x} - \omega_0 t)]$$

$$+(1/2)(\boldsymbol{B}_0 + \boldsymbol{B}_+ + \boldsymbol{B}_-)\exp[i(-\boldsymbol{k}_0 \cdot \boldsymbol{x} - \omega_0 t)] + c.c.,$$

where the wave amplitudes vary slowly in space and time with respect to the scales k_0 and ω_0. Recall that for the linear stability analysis $|\boldsymbol{F}_0|$, $|\boldsymbol{B}_0| \gg |\boldsymbol{F}_\pm|, |\boldsymbol{B}_\pm|$, and the intensities of the pump waves are constant. The linearized equations can then be Fourier transformed in the transverse direction and Laplace transformed over time. When the light-wave amplitudes vary slower than $\langle n \rangle$, the plasma reacts to variations in the fields almost instantaneously. The sound-wave equation becomes

$$\langle n \rangle(\omega, k) = \Gamma(\omega, k)\left\langle \boldsymbol{V}_\perp^2 \right\rangle_L ,$$

where

$$\Gamma(\omega, k) = \left(\omega_e^2/8\omega_0\right)\left[c_s^2 k^2 / \left(c_s^2 k^2 - 2i\gamma\omega - \omega^2\right)\right],$$

and $\langle \boldsymbol{V}_\perp^2 \rangle_L$ contains only linear terms. The line function $\Gamma(\omega, k)$ characterizes the ion-acoustic response of the plasma to the ponderomotive force of the fields. The Fourier transform over the transverse coordinates is equivalent to letting the sidebands $\boldsymbol{F}_\pm$ and $\boldsymbol{B}_\pm$ vary such that

$$|\boldsymbol{F}_\pm| \propto \exp[\pm i\boldsymbol{k}_\perp \cdot \boldsymbol{r}]$$

$$|\boldsymbol{B}_\pm| \propto \exp[\pm i\boldsymbol{k}_\perp \cdot \boldsymbol{r}].$$

In the limit $|\boldsymbol{k}_\perp/\boldsymbol{k}_0| \ll 1$, $\theta \approx |\boldsymbol{k}_\perp/\boldsymbol{k}_0|$ constitutes the small angle or paraxial approximation and restricts this analysis to near-forward and near-backward scattering.

Finally, by keeping only the electromagnetic modes driven resonantly, the linearized equations governing the interaction of the four sidebands are obtained. They take the form

$$LA = MA$$

where $\boldsymbol{A} = (F_-^*, F_+, B_-^*, B_+)^T$ and $L_{ij} = (-\omega \pm i\nu d_x - ck_\perp^2/2k_0)\,\delta_{ij}$. The coupling terms M_{ij} are proportional to $\Gamma(\omega,k)$ and the pump intensities. Each coupling term corresponds to one of the refractive-index gratings that mediate the

interaction of the sidebands. These gratings have components $\langle n\rangle(\omega, 2\boldsymbol{k}_0 \pm \boldsymbol{k}_\perp)$, $\langle n\rangle(\omega, \pm\boldsymbol{k}_\perp)$ and $\langle n\rangle(0, 2\boldsymbol{k}_0)$ along with their complex conjugates. Some of these gratings are shown in Fig. 46.4. Note that the terms ω and $k_\perp^2/2k_0$ act as the linear phase shifts while the M_{ij} correspond to the nonlinear phase shifts.

Convective Gain Spectrum

The four-sideband equations are a system of four coupled complex linear equations. From these equations information about the stability of the four-sideband interaction can be obtained. The convective gain spectrum is obtained by solving these equations as a two point boundary value problem with $B_\pm(L)$ and $F_-(0)$ equal to zero and $F_+(0)$ set at a finite constant value δ. As shown in Fig. 46.5, this process is equivalent to scattering the probe sideband $F_+(0)$ from the system into the four sidebands. In Figs. 46.6(a)–46.6(d) the convective gain of these four sidebands is plotted as a function of $k_\perp^2 L/2k_0$ and $\omega L/v$, where v is the group velocity of the light waves in the plasma. In these plots the gain is scaled to the size of the input probe δ and the pump intensity is 0.92 of the minimal absolute threshold intensity where $|B_0| = |F_0|$.

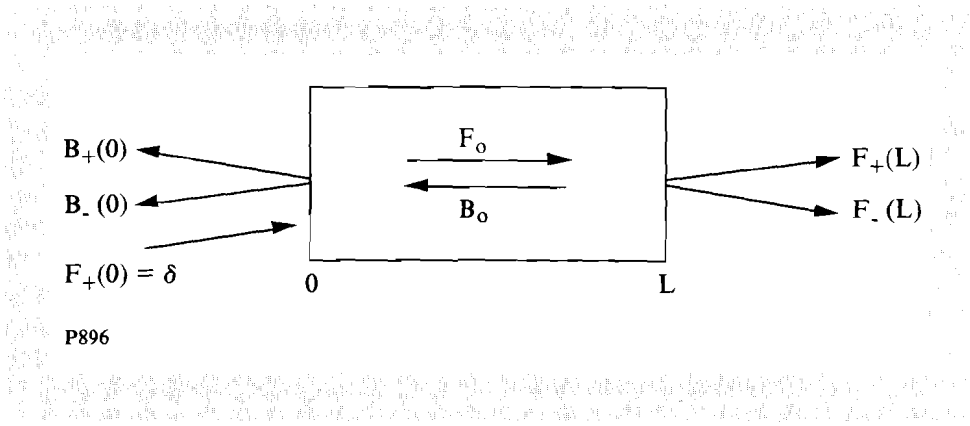

Fig. 46.5
A probe sideband seeds the convective gain and scatters into four sidebands.

In Fig. 46.6(a), the $F_+(L)$ sideband is shown. The surface plot illustrates the gain of the F_+ sideband after one pass through the plasma for a range of input angles and frequencies. Note that gain occurs for this anti-Stokes sideband at two negative values of the frequency shift. These frequencies correspond to ion-sound-wave frequencies of the gratings. The small frequency shift corresponds to scattering from the small-k grating and the larger frequency shift corresponds to scattering from the large-k grating. Their frequency shifts are given by the linear dispersion relation $\omega^2 = c_s^2 k^2$, of the ion-acoustic waves that form the gratings. At the large upshifted frequency, energy is extracted from the F_+ sideband. This is due to the resonantly enhanced interaction of the F_+ sideband with the B_+ sideband through Bragg reflection.

In Fig. 46.6(b) the spectral gain of the B_+ sideband is shown. The shallow periodic structure is due to nonresonant Bragg reflection. Again, the splitting in frequency that occurs for small frequency-shifted gain is due to the

resonant grating at $(\omega, \pm\boldsymbol{k}_\perp)$. The other two structures are present because of the grating at $(\omega, 2\boldsymbol{k}_0 \pm \boldsymbol{k}_\perp)$. The frequency-upshifted gain is caused by resonantly enhanced Bragg reflection. The large frequency-downshifted gain is due to Brillouin-like backward four-wave mixing.

The spectral gain of the Stokes-shifted F_- sideband is shown in Fig. 46.6(c). The gain in this figure represents resonantly enhanced forward four-wave mixing. The small periodic ripples, independent of ω, correspond to the nonresonant forward four-wave-mixing interaction.

Finally, the gain of the B_- sideband forming the phase-conjugate interaction with the F_+ probe is shown in Fig. 46.6(d). It is important to note that the major contribution of the back-scattered light for these parameters comes from this backward four-wave-mixing interaction. This sideband is dominated by light that scatters off-axis and is shifted by the larger ion-acoustic frequency.

This convective gain analysis reveals the complexity of the four-sideband interaction. Only in certain special limits can the four-sideband interaction be simplified to a two-sideband interaction. These limits make sense only in experiments, such as those dealing with phase conjugation, where there is some external control over which modes are seeded and which gratings are driven. In most laser-plasma interaction experiments no such control is possible.

Absolute-Instability Thresholds

As the intensities of the counterpropagating pump waves are increased, the four-sideband interaction becomes absolutely unstable. Absolute instabilities arise when nontrivial solutions of the linear four-sideband equations occur even in the absence of the seed sideband $F_+(0)$. On the top graph of Figs. 46.7(a) and 46.7(b), the thresholds for the absolute instabilities measured in units of convective gain lengths and plotted as a function of the transverse perturbation wave number are shown. For a plasma typical of that produced in the experiments by Young *et al.*,[23] a convective gain length $\gamma_0 L/v = 1$ corresponds to a pump intensity $I_0 \cong 10^{14}$ W/cm^{-2}. The four-sideband system is unstable in the shaded areas.

On the lower graph of Figs. 46.7(a) and 46.7(b), the real part of the perturbation frequency at threshold is plotted. Both figures are calculated for the case of symmetric pumps and show the data for the nonresonant threshold as a solid black line. In a nonresonant medium, a band of wave numbers centered about $k_\perp^2 L/2k_0 = 3.1$ has the lowest absolute-instability threshold. At threshold these modes are not frequency shifted with respect to the pumps. The peak of this band of wave numbers varies with the wavelength of the pump and the scale length of the medium and results from the synchronous coupling of all four sidebands. This is the four-sideband transverse modulational instability. It can be viewed as self-induced diffraction and can lead to filamentation. At large $k_\perp$ this threshold scales as $\pi|F_0|/4|B_0|$, the absolute-instability threshold for phase conjugation. In this large-$k_\perp$ region

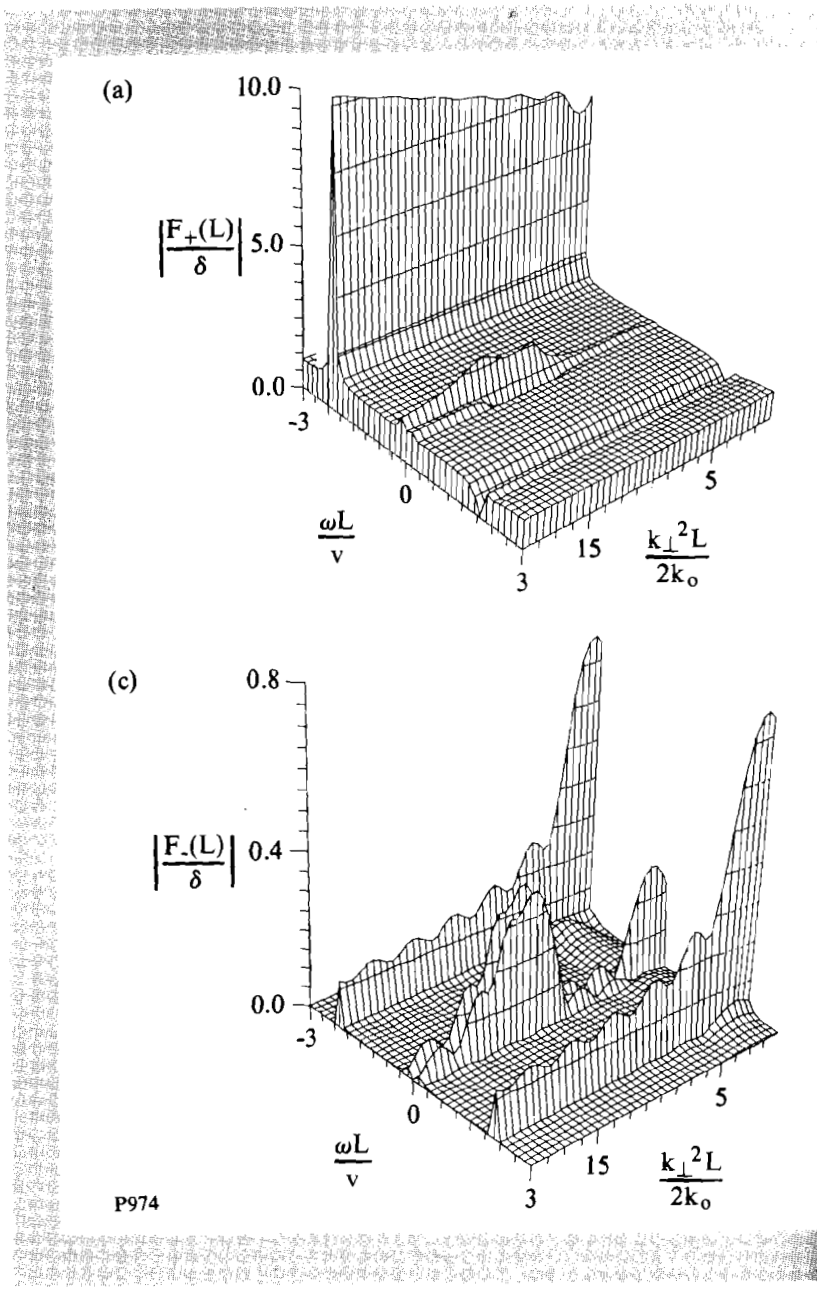

Fig. 46.6
The gain spectrum for the four sideband interaction at $\gamma_o L/v = w_e^2|F_0|^2 L/8\omega_0 v = 0.22$ is seeded by $F_+(0) = 0.001$; $|F_0| = |B_0|$, and $\gamma = 0.05$; (a) F_+, (b) B_+, (c) F^*_-, (d) B^*_-.

the oscillation frequency of the instability at the threshold for absolute instability is proportional to the difference between the pump intensities.

The dashed lines in Figs. 46.7(a) and 46.7(b) are the thresholds for the resonant absolute instabilities. In Fig. 46.7(a) the damping of the ion waves is large enough so that the nonresonant modes still dominate. In Fig. 46.7(b) the ion-acoustic wave damping has been decreased. As a result, the resonant absolute-instability branch has the lowest threshold. In both cases, the resonantly unstable modes have finite frequency shifts at threshold. In Fig. 46.7(a) this frequency shift is precisely the shift associated with the acoustic-wave frequency of the $(\omega, 2\boldsymbol{k}_o \pm \boldsymbol{k}_\perp)$ grating. In Fig. 46.7(b) a splitting about

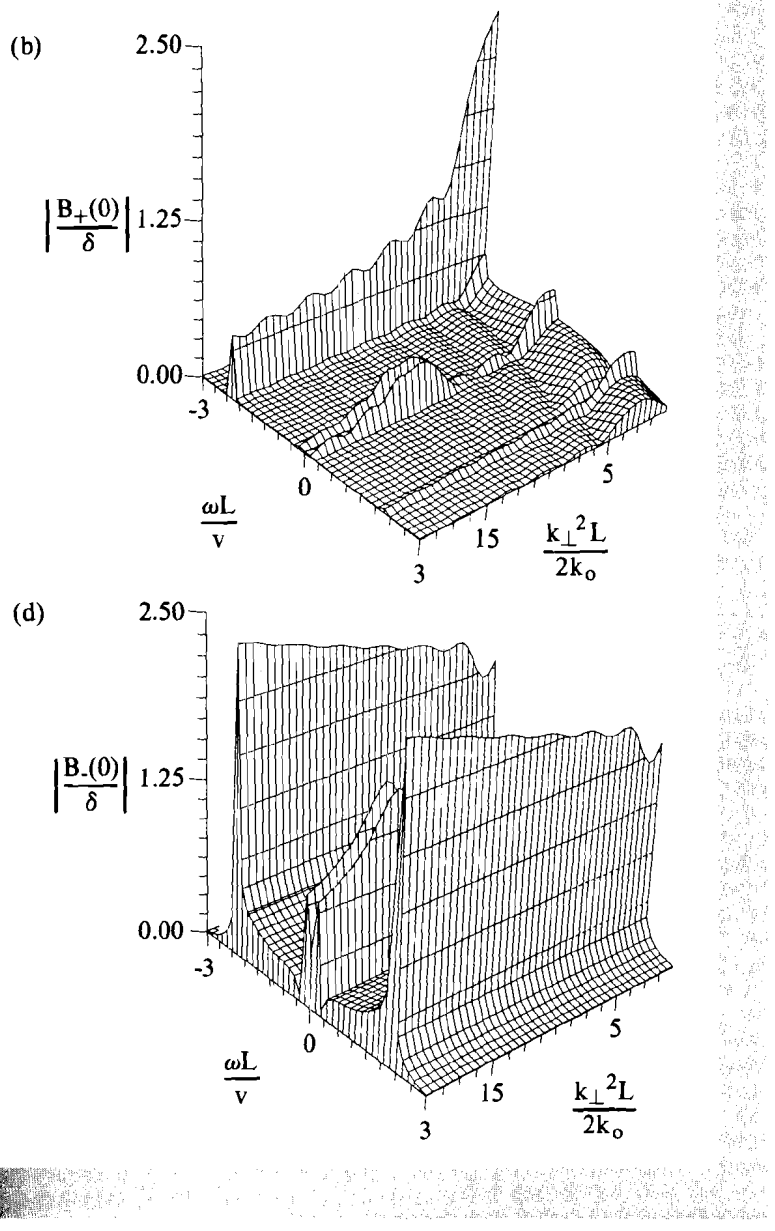

the acoustic-wave frequency can be resolved. Each value of the frequency corresponds to one of the two resonant-threshold curves. Note that neither sign of the acoustic frequency shift is favored in either figure. This occurs because the system is invariant to rotations about the pump axis and both Stokes and anti-Stokes sidebands are retained in the analysis. This symmetry is a fundamental property of the system allowing the sidebands to couple simultaneously through a shared set of gratings. The resonant absolute-instability thresholds approach the phase-conjugate threshold at large $k_\perp$. Goldman and Williams have studied the resonant absolute instability for phase conjugation in inhomogeneous plasmas with asymmetric pumping.[21] Near $k_\perp = 0$, the resonant threshold takes on a hybrid character; a result of a

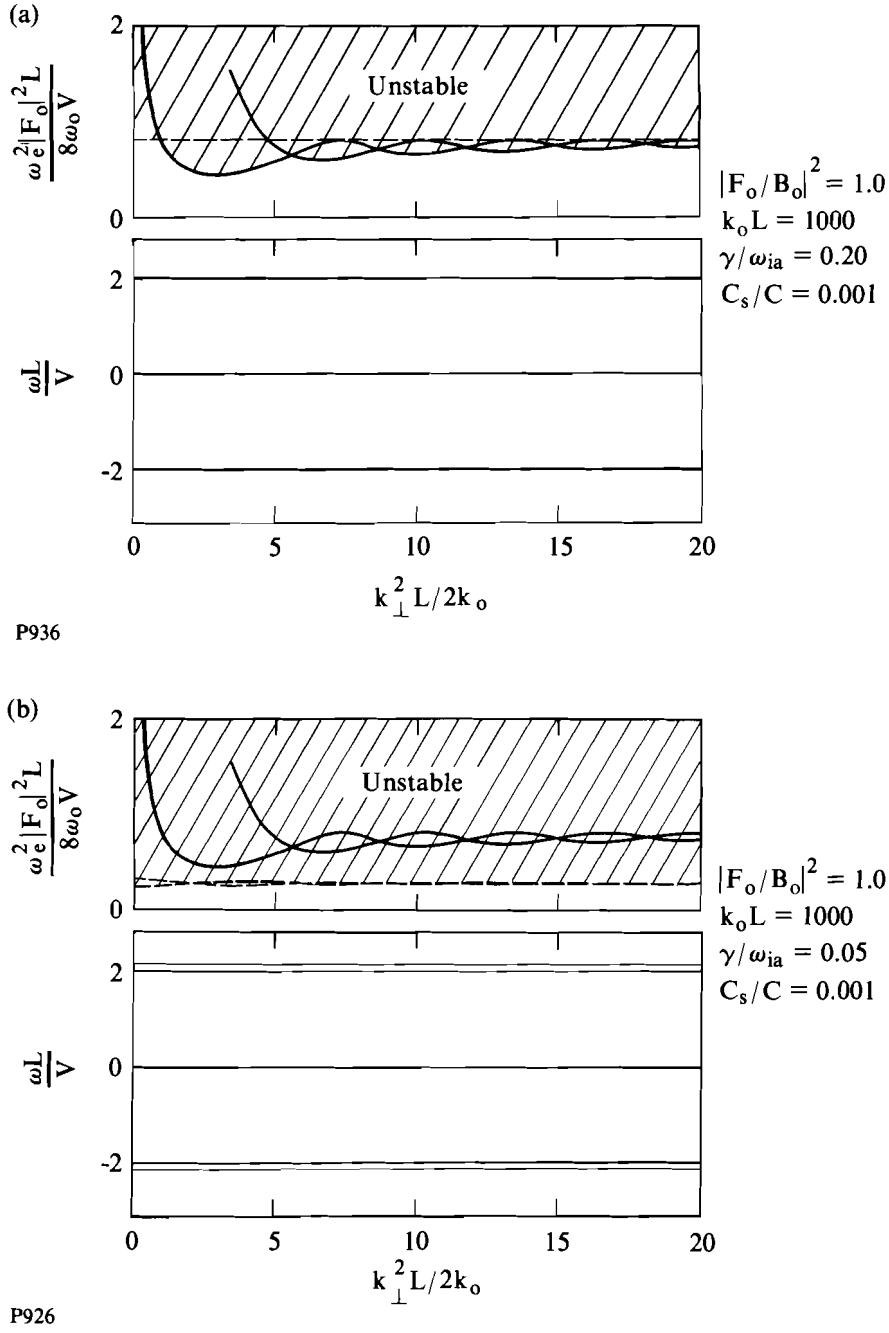

Fig. 46.7
The four-sideband interaction is absolutely unstable in the shaded regions in the top graph, and the frequency of the absolutely unstable sidebands at threshold is shown in the lower graph for each figure. In (a) $\gamma = 0.20$, and in (b) $\gamma = 0.05$. The dashed lines correspond to resonant absolute-instability modes at threshold and the solid lines correspond to nonresonant absolutely unstable modes at threshold.

combination of two-sideband interactions. In fact it is this on-axis resonance at which Fig. 46.7(b) shows the lowest absolute instability threshold.

Since the counterpropagating pump field is only a fraction of the incident pump field in inertial confinement applications, it is of particular interest to know what effect the imbalance of the pump-wave intensities has on these absolute thresholds. In Fig. 46.8 the minimal value of the absolute-instability threshold is plotted as a function of $|B_o/F_o|^2$ for two values of the ion-acoustic wave damping. For the nonresonant threshold, the small-$k_\perp$ threshold is the global minimum until very small values of $|B_o/F_o|^2$ are reached. At these values the large-$k_\perp$ phase-conjugate threshold is the minimum absolute-instability threshold. For $\gamma = 0.2$ the minimal threshold corresponds to the nonresonant curve except at very small values of $|B_o/F_o|^2$. This $\gamma = 0.2$ curve corresponds to $k_\perp = 0$. When $\gamma = 0.05$, the minimal threshold is a result of the resonant threshold and takes on a global minimum at $k_\perp = 0$. The second curve for this value of the ion-acoustic wave damping corresponds to the second threshold at $k_\perp = 0$. In general, the absolute-instability threshold is relatively insensitive to $|B_o/F_o|^2$ until it approaches zero. At $|B_o/F_o|^2 = 0$ the two pumps de-couple and no absolute instabilities can arise. From this figure it is clear that only a fraction of the incident light needs to be back-scattered before the four-sideband instabilities become important.

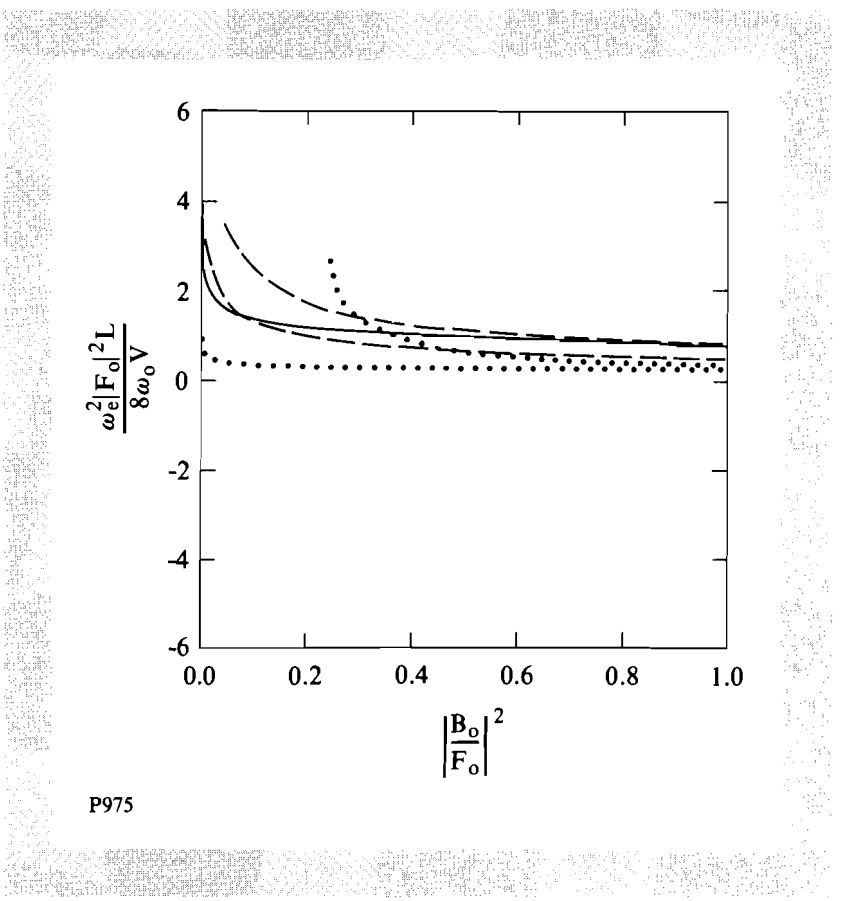

Fig. 46.8
The variation of the minimum absolute-instability threshold with the ratio of backward to forward pump intensity $|B_o/F_o|^2$ is shown. The dashed curves correspond to nonresonant absolute-instability thresholds. The lower dashed curve corresponds to the minimal threshold near $k_\perp^2 L/2k_o = 3.1$, while the higher dashed curve corresponds to $k_\perp^2 L/2k_o = 60.0$. The dotted curves correspond to resonant absolute-instability thresholds at $\gamma = 0.05$ and $k_\perp^2 L/2k_o = 0$. The solid curve corresponds to the resonant absolute-instability threshold at $\gamma = 0.20$ and $k_\perp^2 L/2k_o = 0$.

Discussion

Above the absolute threshold, when the gratings are heavily damped, the four-sideband transverse modulational instability results in conical emission since the instability grows from noise-level seed sidebands that have no preferred orientation. Several recent experiments have been done using nonresonant media exhibiting the characteristics of the four-sideband instability.[24] It is likely that the resonant instabilities will also be identified since they are so closely related to well-known instabilities. For plasma conditions typical of laser-plasma interaction experiments, this simple model predicts threshold intensities of the same magnitude as the intensities typically realized. In fact, these thresholds are much lower than those estimated for the convective-filamentation instability.

The primary near-forward and near-backward scattering instabilities that occur during the interaction of two intense counterpropagating light waves result from the planar four-sideband interactions composed of several distinct one- and two-sideband interactions. A true four-sideband instability occurs when the four sidebands and two pumps are simultaneously phase matched. The four-sideband transverse modulational instability dominates the interaction in nonresonant media. In a plasma the four-sideband resonance is still present, but both the resonantly enhanced phase-conjugate interaction and an on-axis hybrid instability resulting from the simultaneous resonantly enhanced interaction of the two types of forward four-wave mixing are also important. This latter hybrid instability has the lowest absolute-instability threshold for small values of the ion-acoustic wave damping. The instabilities arising as a result of the coupling between counterpropagating waves dominate the single-wave instabilities and require only a fraction of the incident laser to be back-scattered. Thus, the second pump wave increases the number of channels by which the laser energy is converted into unstable modes, increasing the gain of unstable sideband modes.

In laser-produced plasmas of interest for inertial confinement fusion, inhomogeneity, ion inertia, thermal effects, the time dependance of the laser pulse, and velocity gradients of the plasma will all have fundamentally important effects on the four-sideband interaction. As a result, more detailed studies must be carried out before a clear understanding of the role of four-sideband instabilities in ICF emerges.

ACKNOWLEDGMENT

This work was supported by the National Science Foundation under contract No. 9507093, by the U.S. Department of Energy Division of Inertial Fusion under agreement No. DE-FC03-85DP40200 and by the Laser Fusion Feasibility Project at the Laboratory for Laser Energetics, which has the following sponsors: Empire State Electric Energy Research Corporation, New York State Energy Research and Development Authority, Ontario Hydro, and the University of Rochester.

REFERENCES

1. C. E. Max, *Physics of Laser Fusion Volume I:* "Theory of the Coronal Plasma in Laser Fusion Targets," UCRL-53107 (1982).

2. R. L. McCrory and J. M. Soures, *Laser-Induced Plasmas and Applications*, edited by L. J. Radziemski and D. A. Cremers (Dekker, New York, 1989), Chap. 5.

3. J. F. Drake *et al.*, *Phys. Fluids* **17**, 778 (1974).

4. B. I. Cohen and C. E. Max, *Phys. Fluids* **22**, 1115 (1979).

5. W. L. Kruer, *The Physics of Laser Plasma Interactions* (Addison-Wesley, New York, 1988), Chap. 13.7, pp. 168–177.

6. H. A. Rose, D. F. DuBois, and B. Bezzerides, *Phys. Rev. Lett.* **58**, 2547 (1987).

7. D. M. Villeneuve, H. A. Baldis, and J. E. Bernard, *Phys. Rev. Lett.* **59**, 1585 (1987).

8. H. A. Baldis *et al.*, *Phys. Rev. Lett.* **62**, 2829 (1989).

9. I. M. Begg and R. A Cairns, *J. Phys. D: Appl. Phys.* **9**, 2341 (1976).

10. C. J. Randall, J. J. Thomson, and K. G. Estabrook, *Phys. Rev. Lett.* **43**, 924 (1979).

11. C. J. Randall and J. R. Albritton, *Phys. Fluids* **24**, 1474 (1981).

12. P. Narum, A. L. Gaeta, M. D. Skeldon, and R. W. Boyd, *J. Opt. Soc. Am. B* **5**, 623 (1988), and references therein.

13. A. L. Gaeta, M. D. Skeldon, R. W. Boyd, and P. Narum, *J. Opt. Soc. Am. B* **6**, 1709 (1989).

14. F. W. Perkins and E. J. Valeo, *Phys. Rev. Lett.* **32**, 1234 (1974).

15. S. N. Vlasov and E. V. Sheinina, *Izv. Vyssh. Uchebn. Zaved. Radiofiz.* **26**, 20 (1983); *Radiophys. Quantum Electron.* **26**, 15 (1983).

16. W. J. Firth and C. Paré, *Opt. Lett.* **13**, 1096 (1988).

17. G. Grynberg and J. Paye, *Europhys. Lett.* **8**, 29 (1989).

18. W. J. Firth, A. Fitzgerald, and C. Paré, *J. Opt. Soc. Am. B* **7**, 1087 (1990).

19. C. J. McKinstrie and G. G. Luther, *Phys. Scr.* **T-30**, 31 (1990).

20. G. G. Luther and C. J. McKinstrie, *J. Opt. Soc. Am.* B **7**, 1125 (1990).

21. M. V. Goldman and E. A. Williams, "Time-Dependent Phase Conjugation and Four-Wave Mixing in Plasmas," submitted to *Phys. Fluids*, and references therein.

22. H. A. Rose, D. F. DuBois, and D. Russell, *Fiz. Plazmy* **16**, 926 (1990). English language version available as Los Alamos report LA-UR-89-3349.

23. P. E. Young *et al.*, *Phys. Rev. Lett.* **61**, 2336 (1988).

24. A bibliography of related experimental papers is given in Ref. 20.

Section 2
ADVANCED TECHNOLOGY DEVELOPMENTS

2.A Experimental Investigation of Bessel-Beam Characteristics

Previous work by Durnin[1] has shown that the J_0 Bessel function, as an exact solution to the free-space Helmholtz equation, may be of interest in optics. The particular interest in this solution lies in its "diffraction-free" propagation characteristics. That is, the J_0 solution corresponds to the propagation of a very narrow beam (the central portion of the J_0^2 transverse intensity distribution) without transverse spreading over distances exceeding by orders of magnitude the Rayleigh range of Gaussian beams of the same initial FWHM. In the ideal case the electric field of the (zero-order) Bessel beam is given by

$$E(r,\phi,z,t) = a\, e^{i(-\omega t + k_{\|} z)} J_0(k_{\perp} r) ,$$

where the propagation direction is along z, $k_{\|} = (2\pi/\lambda)\cos\theta$, $k_{\perp} = (2\pi/\lambda)\sin\theta$, and θ is a fixed angle to be specified later. However, one should not expect efficient power transport via Bessel beams because of the many side lobes accompanying the central spot.[2–4]

Durnin *et al.*[2,4,5] have also reported some experimental verifications of these predictions. They used a thin metal ring mask illuminated by a HeNe laser placed in the focal plane of a lens, as shown in Fig. 46.9, to generate a near-ideal Bessel beam. In particular, they showed good agreement between the predicted and the experimentally measured transverse and longitudinal-intensity distributions.

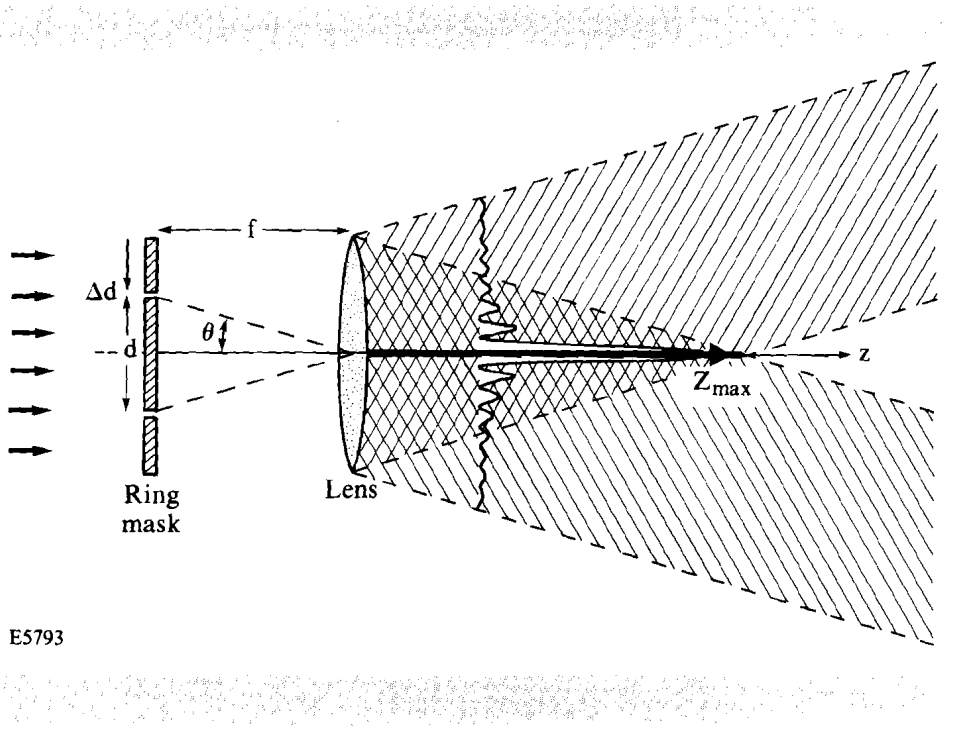

Fig. 46.9
Schematic setup for generating Bessel beams after Durnin *et al.*[1]

An alternative experimental setup was reported by Turunen *et al.*,[6] who used a holographic optical element to generate the Bessel beam. These authors reported 10% power conversion between the input power and the power contained in the Bessel beam. While the cross-sectional intensity distribution closely resembles a J_0 beam, the central peak intensity varied rapidly with distance, with a maximum toward the end of the useful focal range.

Two alternate schemes for generating long-focal-length beams have been suggested by Indebetouw.[7] One scheme uses a Fabry-Perot interferometer to generate a high-quality ring instead of Durnin's metallic ring mask, and the other scheme uses an axicon (a cone-shaped optical element) illuminated with a collimated beam. While the former leads to basically the same results as Durnin's Bessel-beam generator, the latter leads to increasing on-axis intensity with distance from the axicon because of the increase in geometrical annular area contributing to the intensity on axis. This behavior is completely analogous to that in Turunen's setup.[6]

Several authors[8] have attempted to implement various compromises between the features of Gaussian and Bessel beams. In one recent publication Thewes *et al.* attempted to optimize the central spot intensity at the expense of the outer ring intensities.[9] However, any such scheme necessarily limits the distance over which the central beam maintains its nondiffractive properties.

In this article we present experimental data at various laser wavelengths and pulse durations to point out some additional characteristics of Bessel beams beyond those reported so far. In particular, we will show interferometric measurements of the phase front of Bessel beams, typical transverse and longitudinal Bessel-beam profiles, and the extent to which they agree or disagree with predictions. We will also present detailed data on energy content in the Bessel rings. Finally, we will demonstrate that unstable resonators are potential Bessel-beam sources under certain conditions. The experimental results will be compared with both the theoretical (ideal) Bessel-beam predictions as well as with computer simulations using the actual experimental parameters.

Experimental Setup and Results

The Bessel-beam generator setup shown in Fig. 46.9 was used for a number of experiments. In Fig. 46.10 we show a typical transverse Bessel-beam profile using a 1.054-μm, Nd:YLF laser source of ~1-ns pulse duration. The annular ring mask was made from a metal-coated glass substrate into which a ring was etched with a 12.5-mm inner diameter and a 0.1-mm ring width. The lens used to generate the Bessel beam was a 1-m focal-length lens.

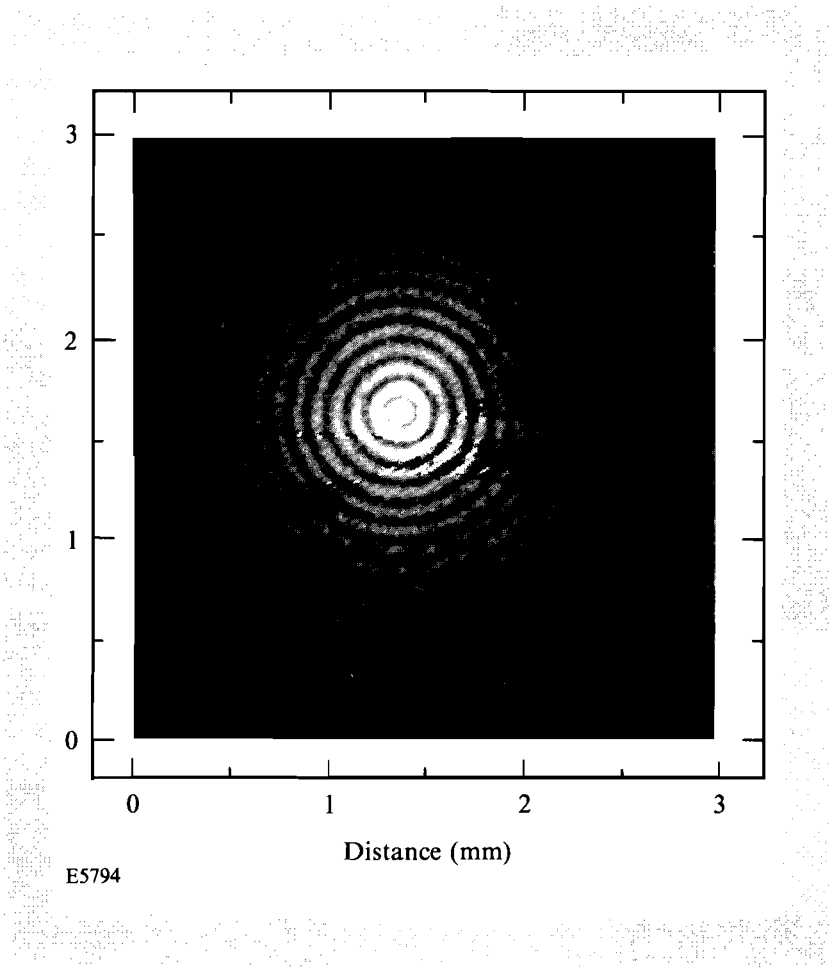

Fig. 46.10
Typical Bessel-beam photograph obtained with a ring aperture of 12.5-mm diameter and 0.1-mm ring width, illuminated by a 1-ns, 1.054-μm, collimated laser pulse from a mode-locked Nd:YLF laser. The photograph is taken at 1 m from the 1-m focal length lens (see Fig. 46.9).

Bessel-beam photographs were taken at several distances from the lens out to 3.75 m from the lens, well beyond the expected geometrical focal range[1,5] for the Bessel beam of $Z_{max} \approx R/[\tan(d/2f)] \approx 2.8$ m. Here, R is the smaller of either the radius of the lens or the "effective" radius of the diffraction pattern cast onto the lens. The effective radius is defined as $R_{eff} = d/2 + f\lambda/\Delta d$, where d and Δd are the diameter and width of the ring aperture, and f is the focal length of the lens. In the above case the focal range of our Bessel beam was limited by the size of the diffraction pattern on the lens ($R_{eff} \approx 17$ mm), whereas the lens radius was 4 cm.

An azimuthal average about the center of symmetry of the Bessel beam in Fig. 46.10 is shown in Fig. 46.11. Also shown in Fig. 46.11 is a J_0^2 curve normalized to an average of the first six side lobes of the transverse intensity distribution. This normalization was found to be the best one based on arguments presented later in this article. We note the general agreement between the experimental data and the ideal J_0^2 intensity distribution. However, we also note that the central maximum is well below the expected value and that the minima in the distribution are not true zeros.

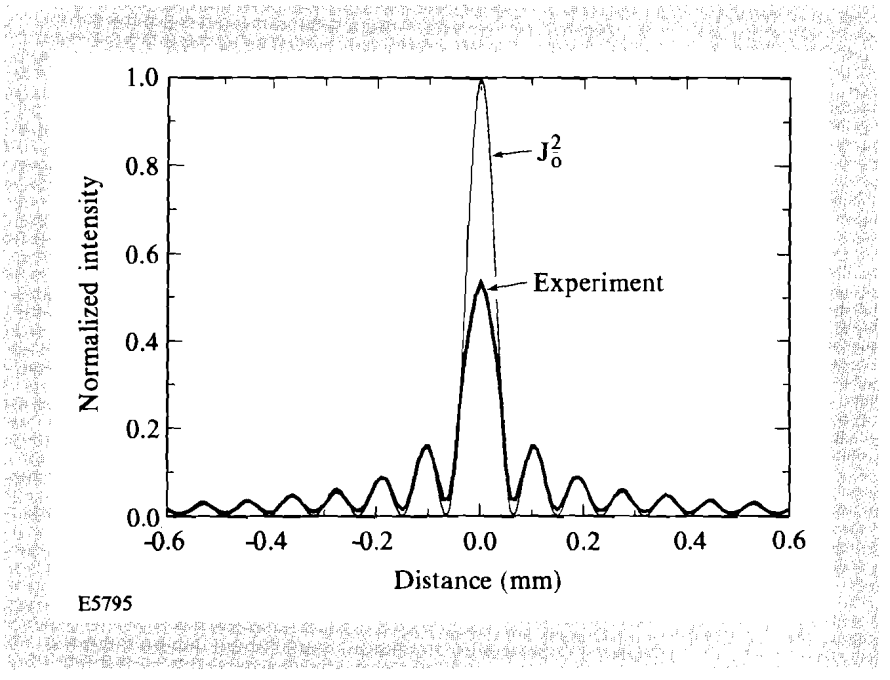

Fig. 46.11
Transverse intensity profile of the Bessel beam in Fig. 46.10 obtained from azimuthally averaging the digitized data in Fig. 46.10.

The data was corrected for film response as determined from separate calibration experiments using the same laser pulses and standard procedures.[10] Thus, film response cannot account for the non-zero minima, nor can film halo effects. We also estimate that the errors inherent in azimuthal averaging (mostly the determination of the exact center of symmetry) cannot account for this discrepancy. However, we note that the image in Fig. 46.10

shows considerable speckle that we attribute primarily to light scattered by the etched ring mask. This scattering is most likely the primary cause for the non-zero minima of the observed Bessel beams as well as the reduced center-peak intensity.

The size of the central lobe, i.e., the diameter of the first zero ring (125±5μm), agrees very well with the predictions ($d_{1z} = 4.81/k_{\perp} \approx 122$ μm). In fact, this good agreement between J_0^2 and experimental transverse intensity distributions holds even well beyond the geometrical focal range Z_{max}, although the overall intensity drops rapidly for $z > Z_{max}$.

From a series of images taken at different distances we have obtained the longitudinal intensity distribution (Fig. 46.12) for the center lobe of the Bessel beam. Figure 46.12 also contains the simulated longitudinal intensity distribution on the basis of numerical Fresnel diffraction simulations. The agreement between experiment and theory is again reasonable. We note that the monotonically decreasing intensity distribution in Fig. 46.12 differs markedly from that shown in Ref. 5 and reproduced in modified form in Fig. 46.13. The difference lies in whether the Bessel-beam propagation at long distances is primarily limited by diffraction from the lens aperture (lens-limited case, Fig. 46.13) or whether it is dominated by the lateral extent of the diffraction pattern from the mask (diffraction-limited case, Fig. 46.12). In the latter case one can think of the lens as being of nearly infinite extent compared to the diffraction pattern cast by the ring aperture.

Figure 46.13 shows the on-axis Bessel-beam intensities for the case where the lens diameter equals the diameter of the ring mask ($R_{lens} = d_{ring} =$ 12.5 mm). The three distributions are for different ring widths. Figure 46.13(a) is typical for a lens-limited Bessel beam generated by a narrow ring width (25-μm) casting a diffraction pattern onto the lens that far exceeds the lens dimensions. As the ring width is increased, the on-axis intensity distribution deviates more and more for ideal Bessel-beam propagation [see Figs. 46.13(b) and 46.13(c)]. Also shown in Fig. 46.13 is the on-axis intensity distribution for a Gaussian beam whose initial FWHM at $z = 0$ equals that of the Bessel beam.

When comparing Figs. 46.12 and 46.13 we note that for a lens of given focal length the focal range of Bessel beams is always larger for the diffraction-limited case (Fig. 46.12) than for the lens-limited case (Fig. 46.13). However, in all cases the focal range of the Bessel beams significantly exceeds that of the Gaussian beams of initially equal FWHM.

A characteristic of Bessel beams is that each ring in the pattern carries approximately the same energy (or power). We have verified this prediction in Fig. 46.14 for the Bessel beam shown in Fig. 46.11. The numerical predictions for the ring energies for this particular experimental setup are practically identical to those made on the basis of J_0^2 and basically agree with the experimental data except for a systematic trend in the center-lobe intensity.

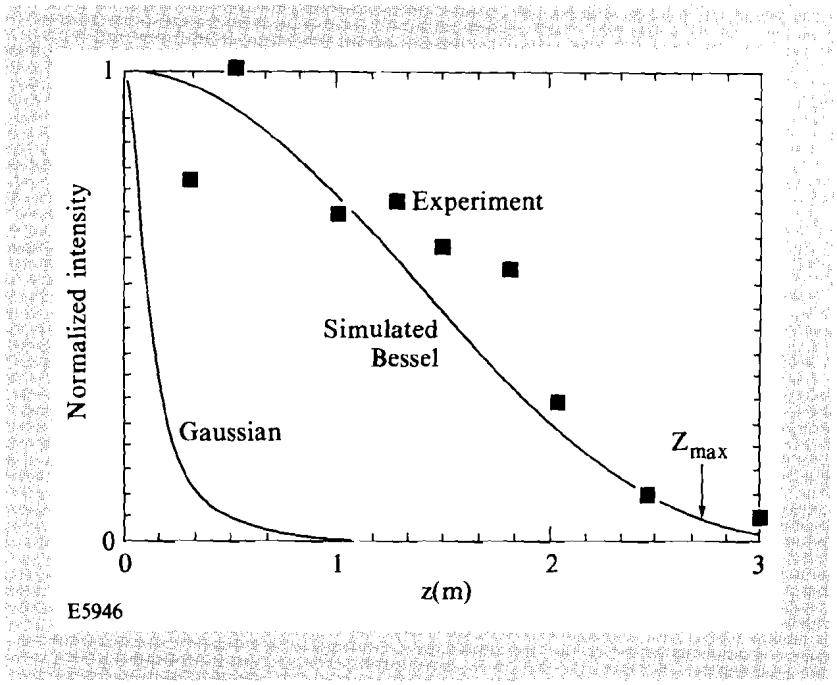

Fig. 46.12
Intensity distribution of the central Bessel lobe along the direction of propagation for the Bessel beam shown in Fig. 46.11. The intensity at long distances is primarily determined by the limited extent of the diffraction pattern of the ring mask rather than the dimension of the lens. Also shown are the predicted intensity distributions on the basis of Fresnel diffraction calculations and the longitudinal-intensity distribution for a Gaussian beam of equal FWHM at the lens.

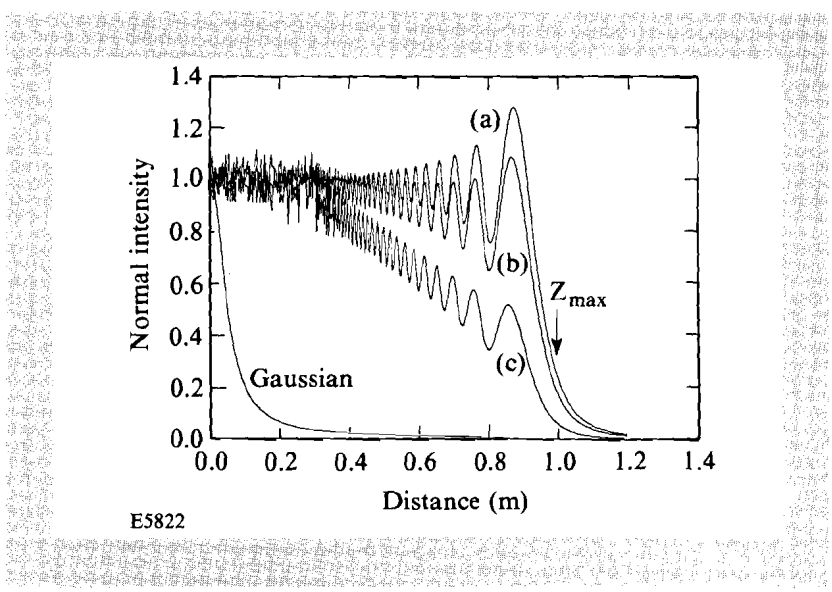

Fig. 46.13
Longitudinal intensity distribution of the central Bessel lobe for lens-limited Bessel beams where the lens diameter equals the ring radius and a ring width of (a) 25 μm, (b) 50 μm, and (c) 100 μm. The ring diameter is 12.5 mm and focal length of the lens is 1 m.

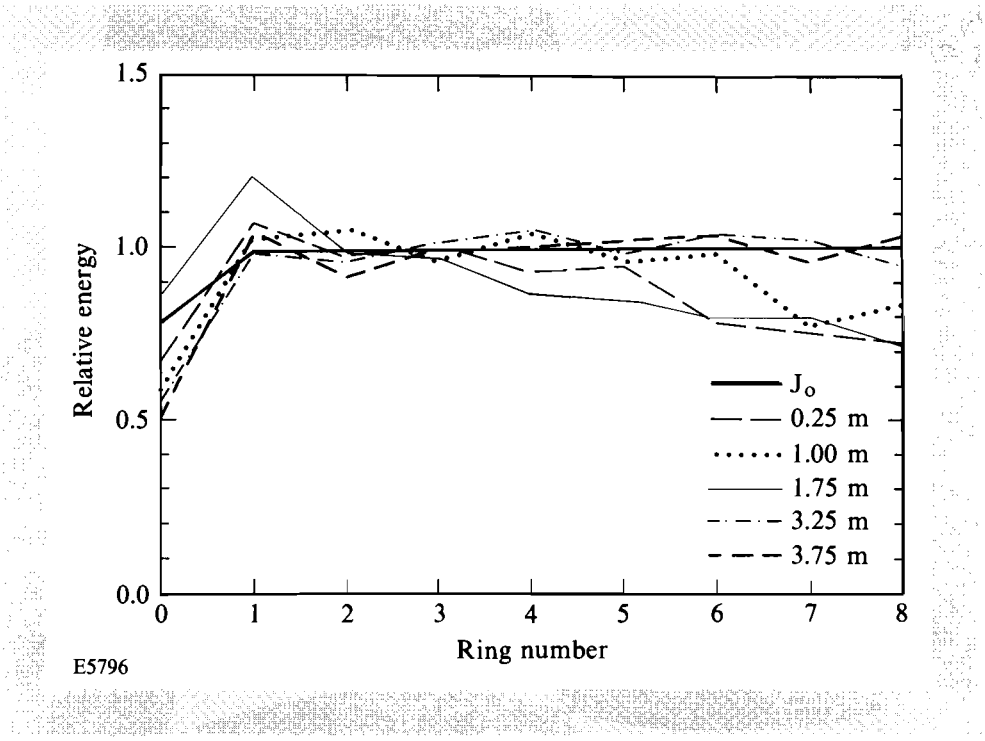

Fig. 46.14
Comparison of theoretical and experimental Bessel-ring energies at various distances along the Bessel-beam propagation. The Bessel beam is the same as that shown in Figs. 46.10–46.13. The systematic deficiency in the experimental energy content of the center lobe is explained by scattering of light at Bessel ring-mask substrate.

There are several potential sources for the low center-lobe intensity. Among them we can rule out film response and saturation, they were accounted for by careful calibration[8] under exactly the same experimental conditions. Similarly, mask asymmetries would have to be so gross as to be easily detected in order to account for the observed decrease in center-lobe intensity. In contrast, scattering within the ring mask with its concomitant phase shifts is expected to significantly reduce the center-lobe intensity, since at the peak of the center lobe all E-fields have to interfere constructively. This condition is fulfilled for the light diffracted from the ring mask, but it is not fulfilled for light scattered by the mask substrate. Consequently, the center-peak intensity can only be decreased by the presence of scattered light.

The regions of zero intensity in the transverse J_0^2 distribution require similarly perfect destructive interference of all the E-fields incident in those regions. Any scattering will invariably lead to non-zero intensities in those regions. However, the zero-intensity regions may also be affected by any mask nonuniformities because of the lack of compensating E-field contributions from different sites on the mask. On the other hand, the maxima of the side lobes, particularly when regarded as azimuthal averages of the intensity distribution, are much less drastically affected. In fact, one can even construct particular cases where the phase shifts associated with the scattered light cancel out to give no net decrease in side-lobe intensity, at least for certain side lobes at certain distances. These arguments therefore justify the normalization of the ideal J_0^2 intensity distributions to an average of the first several side lobes of the experimental intensity distributions (see Fig. 46.11).

An intuitive understanding of Bessel beams is obtained by thinking of a linear combination of plane waves whose wave vectors lie on a cone of opening angle θ. The *x-y* Fourier transform of the electric-field vector of a Bessel beam is a ring, the same ring that generates the Bessel beam in Fig. 46.9. At the same time, the zero-order Bessel beam can be seen as a plane wave with reduced wave vector $k_{||} = k\cos\theta$, as in Eq. (1). The angle θ is given by $\theta = d/2f$, where d is the ring diameter in Fig. 46.9. Since the E-field has opposite signs on either side of its zero values, this corresponds to a π-phase shift in those regions of the otherwise planar phase front of the Bessel beam. A numerical simulation of an interferogram and its experimental counterpart are shown in Fig. 46.15. The phase jumps in the regions of the J_0^2 minima are clearly seen in this figure. Furthermore, we have investigated the phase front of the center lobe of this beam with high accuracy using spatial-synchronous phase detection[11] and we have found that the phase front was planar within the interferometer resolution of λ/80 rms.

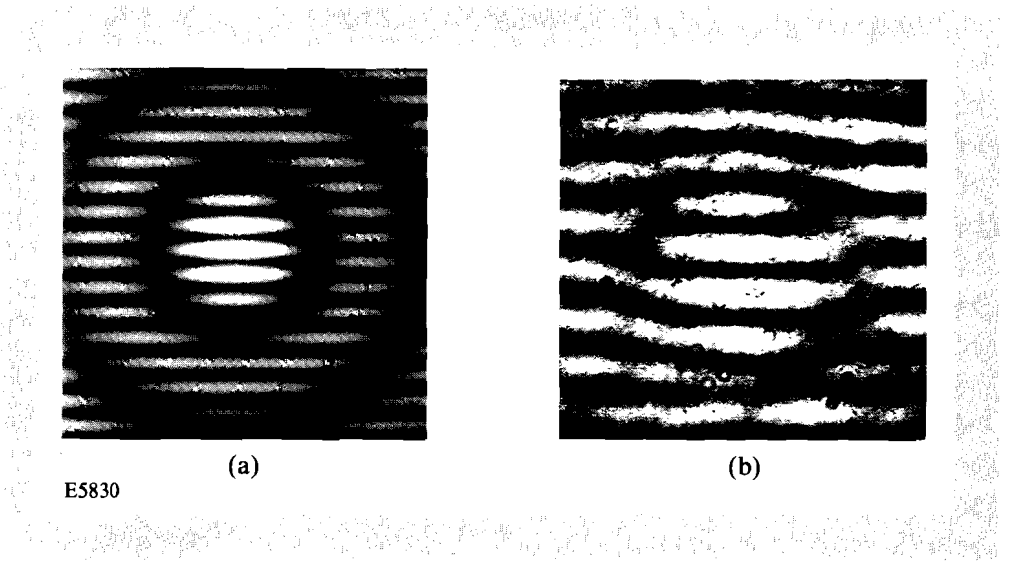

Fig. 46.15
Mach-Zehnder interferograms of Bessel beams. (a) Numerical simulation corresponding to experimental data shown in (b). Note the clearly visible π-phase jumps when crossing the Bessel-beam minima. High-accuracy interferometry of the central spot using spatial-synchronous phase detection has yielded a planar phase front of ≤λ/80 rms.

Two Bessel beams have been generated with the same mask, one at $\lambda_1 = 1.054$ μm (Nd:YLF, pulsed) shown in Fig. 46.10, and the other one at $\lambda_2 = 0.51$ μm (Ar^+, cw) shown in Fig. 46.16. The 0.5-μm Bessel beam clearly shows a three-fold asymmetry in the first few rings while no corresponding asymmetry is apparent in the 1-μm image. This distortion was observed to rotate with the mask; furthermore, the same pattern was observed with a second mask, produced at the same time as the first mask. This pattern also persisted if the mask illumination was changed by moving the illuminating beam over the mask. We attribute this distortion to a variation in ring

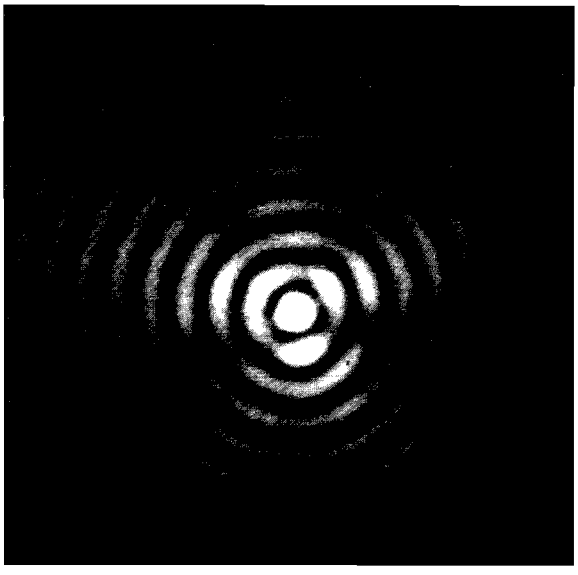

E5829

Fig. 46.16
Transverse intensity distribution of a Bessel beam generated using the same mask as was used for Fig. 46.9 but at $\lambda = 0.51$ μm (cw Ar^+). Note that the clearly visible triangular distortion was observed to rotate with the mask. This distortion is attributed to small deviations from uniform mask thickness of the order of a few microns.

thickness of the mask of a few percent associated with the master pattern that was etched into the gold coating. Unfortunately, this mask error is so small as to be difficult to detect directly; however, blocking part of the ring aperture has been shown to introduce just such intensity asymmetries in the first few side lobes.

Similar asymmetric patterns have been found in numerical modeling of asymmetric ring masks using Babinet's principle by looking at the far-field of a ring mask whose inner disk was placed slightly off-center. With a ring diameter of 12.5 mm and a ring width of 100 μm at a wavelength of 0.5 μm, a 2.5-μm off-center placement of the inner disk clearly accentuates the intensity of the first and second rings on the side opposed to the movement of the inner disk.

Efficient Bessel-beam generation can be obtained with pulsed lasers using an unstable resonator configuration. Such unstable resonators naturally generate ring-shaped beams that loosely approximate the requirements for Bessel-beam generation. An imaging unstable ring-resonator configuration[12,13] is particularly well suited as it images an enlarged version of the scraper mirror onto itself. In practice the sharpness of this image suffers from the finite Fresnel number of the experimental resonator. For this reason we have introduced an additional hard aperture as close to the output as possible in order to reshape the output beam from its original 4.4-mm outer diameter to 3.5 mm; the inner diameter of 2.6 mm remained unchanged. This reduced the output energy by a factor of ~2. However, this Bessel-beam-generation efficiency of ~50% compares very favorably with any of the other experimental values obtained to date. The Bessel beam was then generated with a 7.7-m focal-length lens, which allowed diffraction to fill in the center portion of the beam at the lens. The diameter of the first zero of the Bessel beam was 4 mm and remained unchanged over a distance of ~75 m (see Fig. 46.17). At

the geometrical focal range of ~100 m the Bessel beam was significantly distorted as a result of known phase distortions present in the output beam from the oscillator, although the central spot size was still ~4 mm. A Gaussian beam of the same FWHM would have a depth of focus of twice the Rayleigh range or $2z_R \approx 19$ m. Beyond that distance spreading of the spot is significant whereas the spot size of the Bessel beam remained unchanged over nearly five times that distance. The Gaussian beam would have opened up to a FWHM of ~21 mm at that distance.

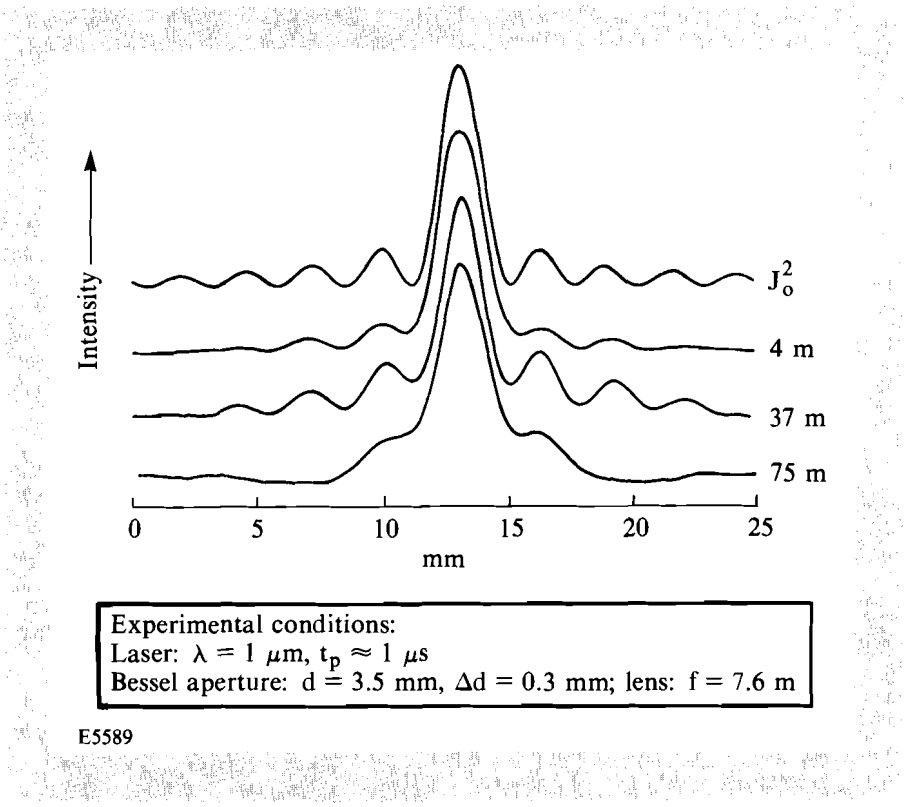

Fig. 46.17
Transverse intensity distribution of Bessel beam generated using the ring-shaped output from an unstable ring Nd:YLF resonator. The J_o^2 distribution shown corresponds to the parameters of the experimental data. The Bessel-beam generation efficiency for this setup is ~50% and could be further improved in an optimized setup.

Conclusions

The size of the central lobe of the Bessel beam as measured by the FWHM of the J_o^2 is typically smaller than either the smallest Gaussian or the smallest Airy disk that can be produced by the same lens. For the purpose of comparison we take a Gaussian with a 1/e-width of its E-field distribution of w_L such that $w_L \approx 3D_{\text{lens}}$ resulting in a FWHM in the focal plane of $D_{\text{Gauss}} \approx 1.13 f^{\#} \lambda$, where $f^{\#}$ corresponds to the f-number of the lens. The corresponding estimates for the Airy disk are $D_{\text{Airy}} \approx 1.01 f^{\#} \lambda$. For the Bessel beam we choose a ring mask of a diameter equal to that of the lens for a setup as shown in Fig. 46.9. The FWHM is then estimated to be $D_{\text{Bessel}} \approx 0.70 f^{\#} \lambda$.

While the FWHM of the Bessel beam is clearly the smallest of the three possibilities to generate small spot sizes with a given lens, the peak intensity is smallest for the Bessel beam. On the other hand, the depth of focus, i.e., the length over which neither spot size nor peak intensity changes appreciably, is by far the largest for the Bessel beam.

Thus, for applications where depth of focus and beam definition (spot size) are of prime importance, Bessel beams present significant advantages over Gaussian beams or Airy spots. Such applications certainly encompass long-distance alignment aids or material processing of poorly defined surfaces (machining or direct-write lithographic applications), when laser power is not of prime concern, but beam definition is. Most Bessel-beam applications probably involve nonlinear processes, or detectors or processes with a threshold response.

Our present investigations have shown that good-quality Bessel-beam generation requires avoidance of scattering problems or other phase distortions impressed on the beam by the ring mask in Fig. 46.9 or any equivalent setup (see, e.g., Ref. 5).

Our phase-front measurements of Bessel beams confirm their basic planar-wave character albeit with π-phase jumps between adjacent rings.

High-quality central Bessel spots of predictable intensity can only be obtained for experimental setups that carefully avoid scattering inside the mask. While small imperfections in ring thickness and circularity affect the rings around the central lobe quite strongly (particularly the zero-intensity regions), they affect the central lobe to a lesser degree.

ACKNOWLEDGMENT

This research was partially supported by the Research Technology Corporation, and by the Laser Fusion Feasibility Project at the Laboratory for Laser Energetics, which has the following sponsors: Empire State Electric Energy Research Corporation, New York State Energy Research and Development Authority, Ontario Hydro, and the University of Rochester.

The authors would like to thank T. Kessler for his help with the experiments and for numerous discussions. We also acknowledge helpful discussions with C. R. Stroud.

REFERENCES

1. J. Durnin, *J. Opt. Soc. Am. A* **4**, 651 (1987).
2. J. Durnin, J. J. Miceli, Jr., and J. H. Eberly, *Opt. Lett.* **13**, 79 (1988).
3. P. Sprangle and B. Hafizi, *Phys. Rev. Lett.* **66** (1991).
4. J. Durnin, J. J. Miceli, Jr., and J. H. Eberly, to appear in *Phys. Rev. Lett.* **66** (1991).
5. J. Durnin, J. J. Miceli, Jr., and J. H. Eberly, *Phys. Rev. Lett.* **58**, 1499 (1987).
6. J. Turunen, A. Vasara, and A. T. Friberg, *Appl. Opt.* **27**, 3959 (1988).
7. G. Indebetouw, *J. Opt. Soc. Am. A* **6**, 150 (1989).

8. F. Gori, G. Guattari, and C. Padovani, *Opt. Commun.* **64**, 491 (1987); E. A. Iolynkina, E. A. Lbragimov, and T. Usmanov, *Sov. J. Quantum Electron.* **18**, 1509 (1988); L. Vicari, *Opt. Commun.* **70**, 263 (1989); M. Zahid and M. S. Zubairy, *Opt. Commun.* **70**, 361 (1989).

9. K. Thewes, M. A. Karim, and A. A. S. Awwal, OSA 1990 Annual Meeting, Boston, MA, *Technical Digest* **15**, 223 (1990), paper ThRR4; S. R. Jahan and M. A. Karim, *Opt. Laser Technol.* **21**, 27 (1989).

10. D. R. MacQuigg, *Appl. Opt.* **16**, 2028 (1977).

11. LLE Review **31**, 114 (1987).

12. A. E. Siegman, *Lasers* (University Science Books, Mill Valley, CA, 1986), p. 901.

13. D. Y. Park, W. Seka, Y. Lin, and D. L. Brown, *Proc. Int. Conf. Lasers '89* (STS Press, McLean, VA, 1990), pp. 449–456.

2.B X-Ray Imaging with Kirkpatrick-Baez Microscopes

This article describes the design, testing, and use of Kirkpatrick-Baez (KB) x-ray microscopes on OMEGA. These microscopes consist of grazing-incidence mirror pairs arranged to reflect and focus x rays, thereby providing images of the x-ray-emitting region. KB microscopes are one of several practical devices that can be used to focus and collect x rays. Simpler x-ray-imaging devices are the pinhole camera and cameras involving coded-aperture (typically Fresnel zone-plate) techniques.[1] These, however, do not use x-ray optics. The KB microscope[2] and its axially symmetric relative, the Wolter microscope,[3,4] both use the principle of grazing-incidence reflection of x rays to form images of the x-ray-emitting region.

The KB microscope was originally conceived and developed by Kirkpatrick and Baez in 1948.[3] In this device, shown in Fig. 46.18, the meridianal rays from a point p are reflected from a mirror surface and form an image at q. For a source-to-mirror distance of d and a mirror-to-image distance of D, the requirement for focusing is given by

$$1/d + 1/D = 2/R\sin i = 1/f. \quad (1)$$

Since only the meridianal rays (i.e., the rays in the plane of Fig. 46.18) are focused by one such mirror, to obtain images of two-dimensional objects, two such mirrors are placed with their normals perpendicular to each other (along x and y) and perpendicular to the source-mirror direction (z-axis). This allows the unfocused sagittal rays of the first mirrors, which are then the meridianal rays of the second mirrors, to be focused. The principal contributions to aberrations of this system are obliquity and spherical aberration.[5]

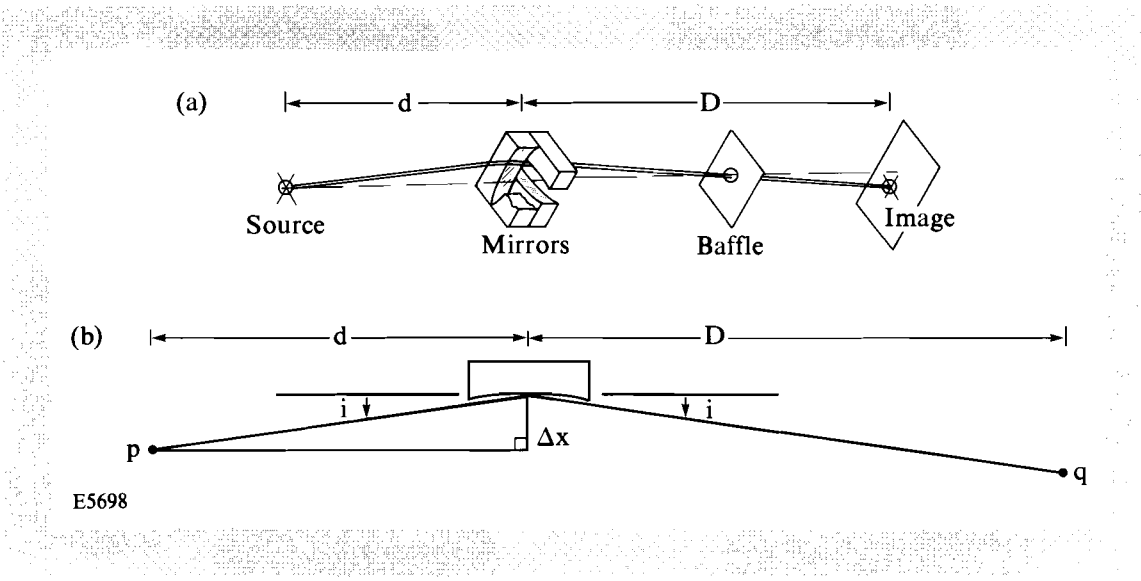

Fig. 46. 18
Schematic of the LLE KB microscope optical assembly (a) and focusing geometry (b).

KB Microscope Development at the Laboratory for Laser Energetics (LLE)

The mirrors of the LLE KB microscope are constructed of Cervit, a glass with a low coefficient of expansion. The assembly of the optical components has been accomplished as follows:[6] The mirrors were cut to shape with their surfaces given a sufficient polish to enable optical contacting to be accomplished at a later stage. Next, the mirrors were arranged on a spherical polishing table, where they were given a radius of curvature of approximately 30 m. Subsequent to initial polishing, the mirrors were given a final surface finish by repeated hand polishing until the surface roughness was <10 Å. This step caused slight changes in the radius of curvature of the mirrors, so that the final focus of the x-ray microscopes had to be determined by actual measurements. The final assembly procedure required that the components of the KB microscope be optically contacted together. The precision of the assembly of the mirror components of the microscope is such that an alignment of better than 1 arc sec is maintained between the mirror normals. This ensures that the amount of misfocus is negligible when compared to spherical aberration and obliquity.

Both nickel-coated and gold-coated KB mirrors have been prepared by the evaporative method. The calculated reflectivities, assuming 0.7° grazing angle, are shown in Fig. 46.19. Both curves include transmission through a 25-μm-Be light shield, which is typical. The nickel-coated mirrors are seen to have a high efficiency at low energies but have a cutoff energy of ~4.5 keV. The gold-coated mirrors, on the other hand, do not have as high an efficiency as the nickel-coated mirrors but have a response that extends out to 7 keV.

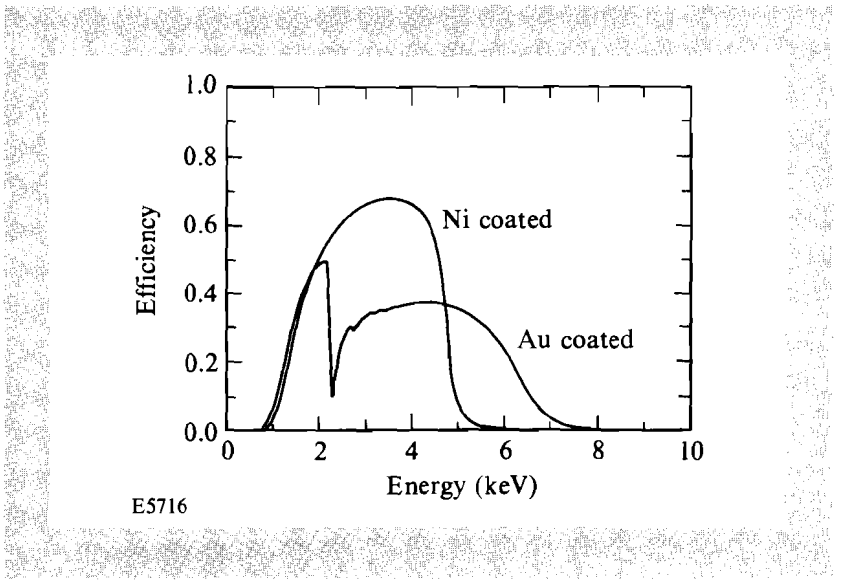

Fig. 46.19
Calculated reflection efficiency of the nickel-coated and gold-coated KB microscopes. Both curves assume an 0.70° grazing angle and include transmission through 25.4 μm of Be, which is used as a blast shield.

KB Microscope Testing

A facility has been assembled at LLE for testing and characterizing KB microscopes. The facility (Fig. 46.20) consists of a two-chamber vacuum system for housing the x-ray microscope and a high-flux electron-beam-generated x-ray source. Both chambers are pumped to an initial vacuum pressure of ~0.1 mTorr by a roughing pump. The chambers are then pumped

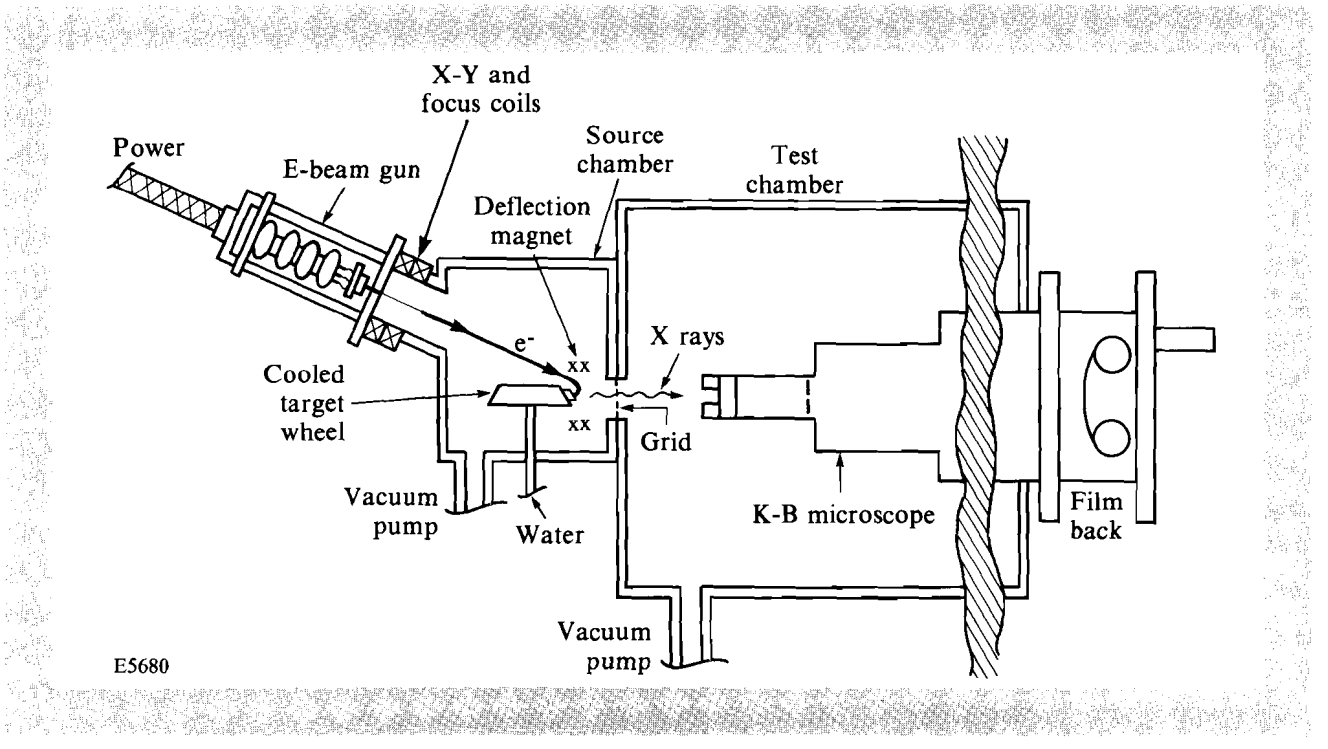

Fig. 46.20
Schematic of the KB microscope testing facility.

to a high vacuum ($<10^{-6}$ Torr) by separate ion pumps, a 500-l/s-capacity pump for the main chamber and a 50-l/s-capacity pump for the x-ray source chamber. X rays are generated by causing an electron beam to strike a metal target positioned inside the source chamber. The electron beam gun is a modified Pierce type.[7] It creates a beam of electrons that can be focused to a spot <1 mm in diameter. The e-beam gun, controls, and power supplies were originally built and sold commercially as a welding device. To direct the e-beam so it strikes the target at the desired position, the operator adjusts the current to the *x*-*y* deflection coils and the bending magnet (Fig. 46.20). Positioning is accomplished visually by aligning the fluorescing spot the e-beam creates on the surface of the target with the previously aligned crosshair of an inspection microscope (not shown in Fig. 46.20). This inspection microscope has been prealigned so that its crosshair and the x-ray microscope are both pointed at the same place on the target wheel. The beam spot size is then adjusted by changing the current supplied to the focusing coil so that an area source of x rays is created. The e-beam gun can be operated at up to 15 kV and 30 amps. Actual beam current depends on specific settings, 10 mA is a typical example. The e-beam is directed onto the source wheel containing several metallic targets on a water-cooled base. Aluminum, iron, and silicon targets are typically used in tests. A summary of typical operating conditions and settings is given in Table 46.II.

Table 46.II: Test chamber x-ray source.

Type	Electron beam, modified Pierce electron gun
	Water-cooled target wheel with focus coil and *x* and *y* deflection fields
Power supply:	0–15 kV
	0–30 amp dc
Filament:	Tungsten
Targets:	Al, Fe, Si, . . .
Typical settings:	8 kV, 17 amp, 10-mA filament current
Bending magnet:	Fe with induced field ~ 10–20 Gauss
Film types used:	Kodak 2495 and Kodak DEF
Exposure time:	10 min to 2 h

E5914

Figure 46.21 shows images obtained on test exposures of a Ni-coated KB microscope. Figure 46.21(a) shows an exposure taken of x rays transmitted through a wire mesh consisting of 25-μm wires on 50-μm spacings when the microscope was arranged at a magnification of ~5.2. Variations in the brightness are caused by spatial variations in the intensity of the e-beam at the target plane. Also, variations in the image quality can be seen to be a function of position in the image. An image of the same grid [Fig. 46.21(b)] was taken at a magnification of 11.0. Again image quality is a function of position in the image.

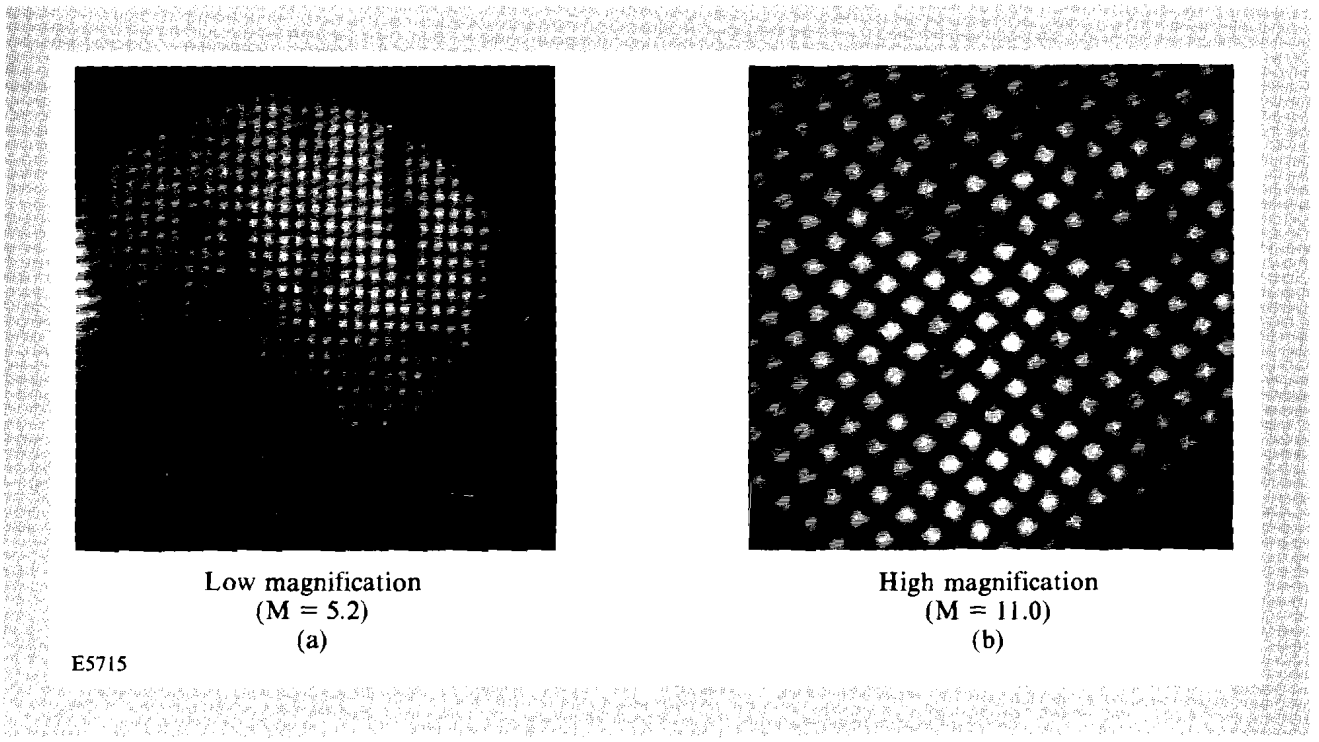

Fig. 46.21
Exposures of back-lit 25-μm wire mesh at magnification of 5.2 and 11.0.

The variation of image quality versus position was analyzed by digitizing the images of Fig. 46.21 and subsequent computer analysis. Lineouts are taken along the axes of the wire mesh. By measuring the width of the shadow of each wire, the resolution at that point in the image plane of the microscope is determined. Figure 46.22 shows plots of the resolution for the Ni-coated KB at both magnifications. We see that the best resolution obtained is ~5 μm and that the field of view is ~500 μm.

The depth of field of the KB microscope was investigated by taking exposures of the wire mesh and varying the mirror-to-film distance D. Figure 46.23 shows a plot of the best resolution obtained from each such distance as a function of change in D. The best resolution is obtained at the optimum focal position. This determination of the optimum value of D serves to characterize the focus equation [Eq. (1)], since for a fixed source-to-mirror distance d and an optimized value of D, the value of the product $R\sin i$ can be inferred. The depth of field of the KB microscope is seen to be ~1 mm.

Summary

The KB microscopes have been used on the OMEGA target chamber for a number of years.[8,9] Originally, two microscopes with nickel-coated mirrors each provided four independently filtered images from the four corners of the mirror assembly [see Fig. 46.18(a)]. The microscopes were placed to view target x-ray emission from two nearly perpendicular views. Testing of the KB microscopes confirms early measurements that the

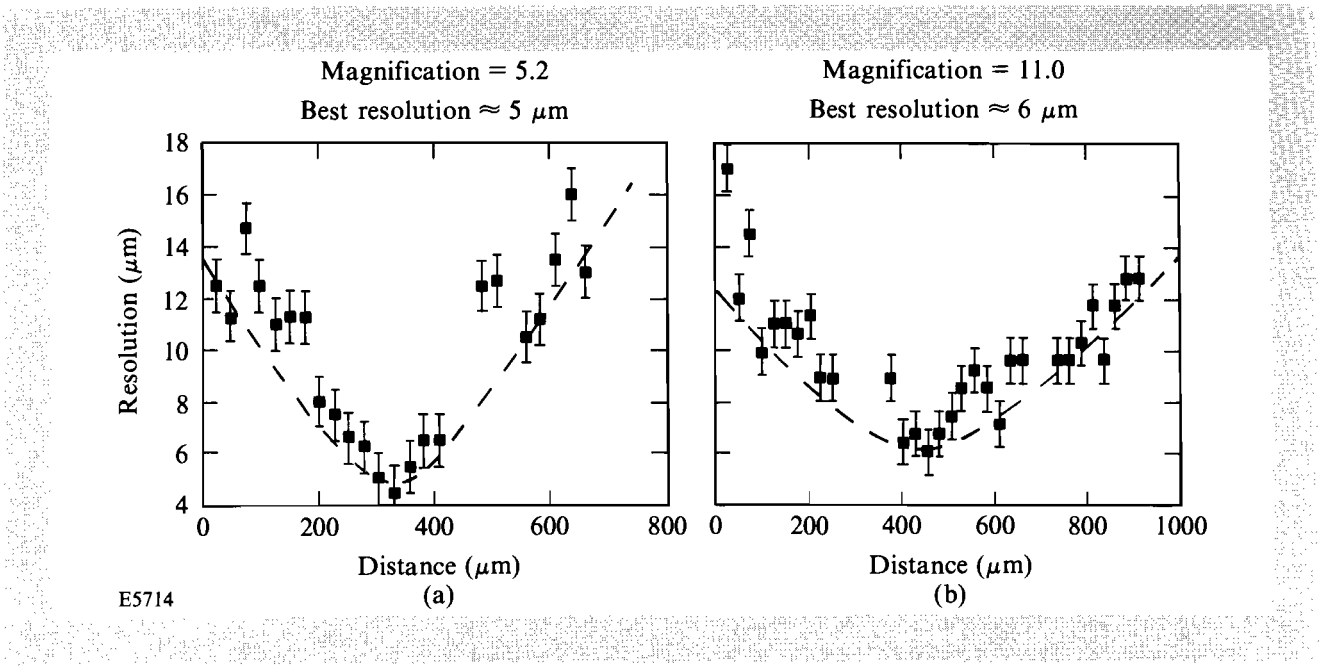

Fig. 46.22
Plots of the resolution versus position as determined from the images of Fig. 46.21.

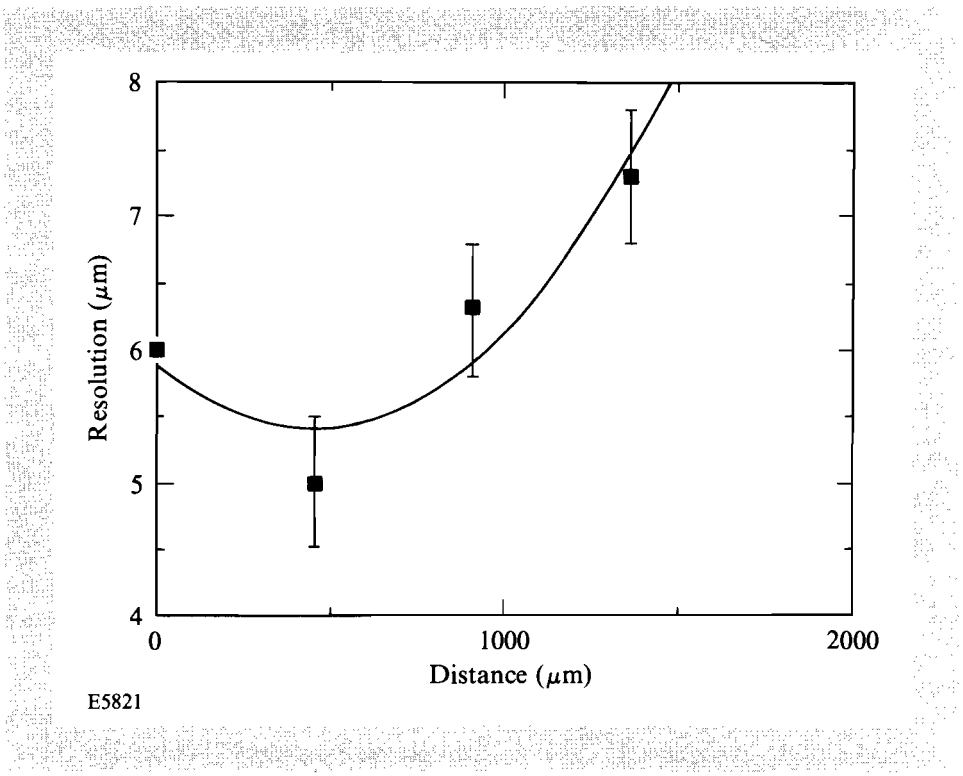

Fig. 46.23
The depth of field and optimum focus are determined by adjusting the mirror to image plane D.

optimum resolution is ~5 μm and that the field of view and depth of field are ~500 μm and ~1 mm, respectively. Recently a new KB microscope assembly with gold-coated mirrors has been completed. The resolution of the Au-coated mirrors allows imaging of x rays up to ~7 keV. This microscope has also been configured with a transmission grating placed at the baffle [Fig. 46.18(a)] in order to obtain imaged spectra of implosion cores. Work on analyzing spectra from dispersed core images is now in progress.[10] The current existing complement of KB microscopes and their parameters are summarized in Table 46.III.

Table 46.III: OMEGA KB microscope parameters.

Ni-coated mirror microscopes:	2
Au-coated mirror microscopes:	1(with transmission grating)
Grazing angle:	~0.7°
Magnification:	5–12
Solid angle:	$\sim 3 \times 10^{-7}$ sr
Sensitive range:	1–7 keV
Number of images:	4/microscope
Film:	Kodak 2495 and Kodak DEF

E5915

ACKNOWLEDGMENT

This work was supported by the U.S. Department of Energy Division of Inertial Fusion under agreement No. DE-FC03-85DP40200 and by the Laser Fusion Feasibility Project at the Laboratory for Laser Energetics, which has the following sponsors: Empire State Electric Energy Research Corporation, New York State Energy Research and Development Authority, Ontario Hydro, and the University of Rochester.

REFERENCES

1. G. H. McCall, *X-Ray Imaging* (SPIE, Bellingham, WA, 1977), Vol. 106, pp. 2–7.
2. P. Kirkpatrick and A. V. Baez, *J. Opt. Soc. Am.* **38**, 766 (1948).
3. H. Wolter, *An. Physik.* **10**, 94 (1952a).
4. H. Wolter, *An. Physik.* **10**, 286 (1952b).
5. J. F. McGee and J. W. Burrows, *X-Ray Imaging* (SPIE, Bellingham, WA, 1977), Vol. 106, pp. 107–112.
6. All of the KB microscope assemblies currently used at LLE were assembled by H. Graf, a former employee of the Institute of Optics of the University of Rochester and now a consultant of Sydor Optics Inc., also of Rochester, New York.

7. F. Rosebury, *Handbook of Electron Tube and Vacuum Techniques* (Addison and Wesley, Reading, MA, 1965), pp. 435–438.

8. M. C. Richardson, R. S. Marjoribanks, S. A. Letzring, J. M. Forsyth, and D. M. Villeneuve, *IEEE J. Quantum Electron.* **QE-19**, 1861 (1983).

9. M. C. Richardson, G. G. Gregory, R. L. Keck, S. A. Letzring, R. S. Marjoribanks, F. J. Marshall, G. Pien, J. S. Wark, B. Yaakobi, P. D. Goldstone, A. Hauer, G. S. Stradling, F. Ameduri, B. L. Henke, and P. A. Jaanimagi, in *Laser Interaction and Related Plasma Phenomena*, edited by H. Hora and G. H. Miley (Plenum, New York, 1986), Vol. 7, pp. 179–211.

10. F. J. Marshall, private communication.

2.C Phase Noise in Mode-Locked Laser-Pulse Trains

Many experiments in laser fusion and other areas require synchronized lasers of different pulse durations. Usually this implies generating pulses in separate laser oscillators. The problem then becomes one of synchronizing two or more actively mode-locked laser-pulse trains, each of which is typically affected by its own timing fluctuations or phase noise. In order to overcome this problem, some form of active timing control is desired. Although characterization of noise in mode-locked lasers has been reported in the literature,[1] there has been little direct discussion identifying the possible sources of this phase noise.

The origin of phase noise in typical laboratory lasers is usually not directly related to any fundamental source, but is a result of the mechanics of their construction. Of course, this does not imply a lack of care by those who build lasers, but merely reflects the general sensitivity to perturbations of laser oscillators. Since noise sources are dependent on the details of the individual laser design, general statements about their origin cannot easily be made. Statements about noise based on material properties or common designs, however, are useful, at least for those using similar materials and designs. In this article we discuss phase-noise problems typically encountered in a 100-MHz, cw mode-locked, Nd:YLF laser running at $\lambda = 1.053$ μm. The laser is acousto-optically mode locked and built on an invar table. The cavity has a simple two-mirror stable design producing 80-ps pulses.

Phase-Noise Spectrum

The bulk of the phase noise in solid-state lasers of this type is below 10 KHz.[2] Within this range, the phase-noise spectrum can be divided into two components, which may be described as acoustic (or vibrational) and thermal. The division is appropriate not only because of the different origins and time scales but also because of the techniques used to make the measurements and to the degree in which they affect an experiment. In

high-repetition-rate experiments, for example, the slowly varying thermal effects are usually of little concern compared to acoustic perturbations, while in low-repetition-rate laser-fusion experiments the potentially larger magnitude of thermal drifts can become important. Both vibrational and thermal sources can cause changes in the length of the laser cavity and these lead to timing jitter. Thermal effects can also cause phase changes through other mechanisms within active components in the laser.

Thermal Effects

Thermal phase noise or drift occurs on a time scale dependent on the thermal mass of the elements and on the temperature characteristics of the environment. In addition, the thermal response of the laser also depends on the thermal load supplied to the laser rod by the flash lamps and the rf power dissipated in the mode locker. Acousto-optic mode lockers are particularly sensitive to temperature changes since they are resonant devices. Figure 46.24 shows the effect of increasing the input power, or thermal load, to a commercial mode locker with a coolant temperature of 20°C. This device is normally used at 10-W input rf power.

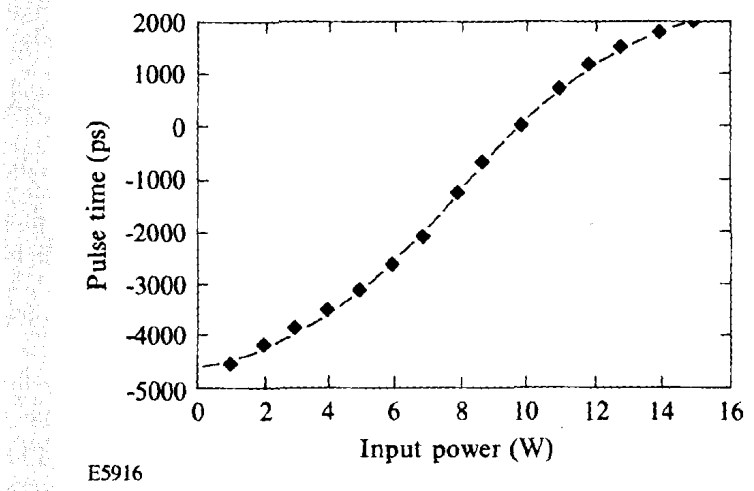

Fig. 46.24
Increasing the input rf power to the mode locker increases its internal temperature, causing a shift in the phase of its acoustic standing wave as it sweeps through resonance. The resonance occurred at about 8-W input rf for a 20°C coolant temperature.

At resonance, the slope is 700 ps/W (rf). Thus for a stability of, say, 10 ps, the input rf power has to be stable to <0.14%, assuming no other sources. Figure 46.25 shows the mode locker's temperature dependence for a constant input power of 10 W. The laser-pulse time versus temperature has a slope of 350 ps/°C. The mode-locker temperature must therefore be stable to < 0.03°C to achieve 10-ps timing stability.

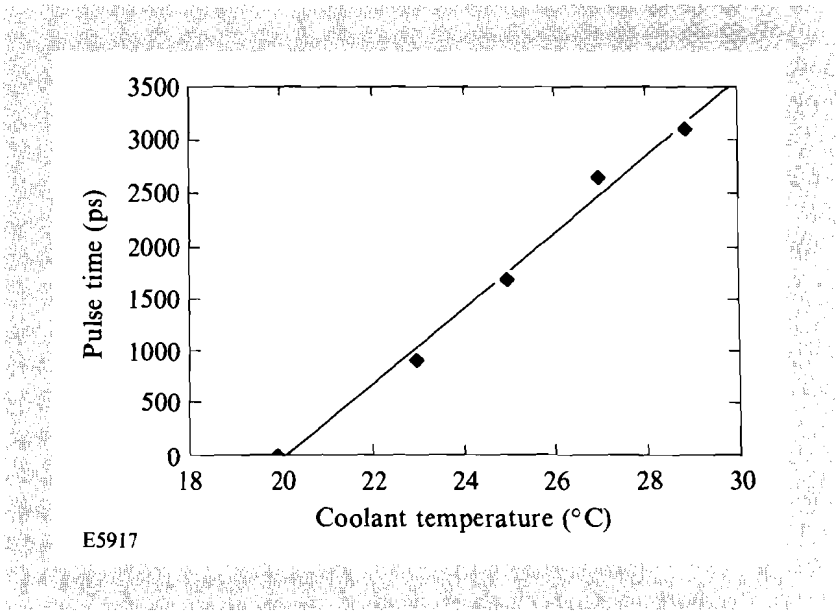

Fig. 46.25
This graph shows the laser-timing shift due to a change in the mode locker's water-bath temperature. Thermal effects in an acousto-optic mode locker can produce huge timing shifts compared to the laser pulse width.

From these results we can see the basis for a technique that uses changes in input rf power to stabilize the mode-locker acoustic-resonance frequency to the rf drive frequency. At 10-W rf, a change in input rf power of 1% is approximately equivalent (thermally) to a coolant temperature change of 0.2°C. Thus small adjustments to the input rf power can be effective in stabilizing the mode locker's temperature and, therefore, its resonance frequency and acoustic wave phase.

It is important to remember that these results depend somewhat on the detailed design of the mode locker. The pulse time versus temperature slope depends on the acoustic Q of the resonant device and on the thermal properties of the optical material used (fused silica in this case). However, results for other devices should be similar.

Acoustic Effects

While thermal effects are on a time scale of seconds to hours, we will consider acoustic or vibrational effects in the frequency range of 1 Hz to 10 KHz or greater. The terms will include any mechanical movement within this bandwidth that induces an optical-path-length change in the laser cavity. Thus, they include effects caused by material index changes as well as those based on physical length changes.

Before continuing with noise sources, the link between cavity length and pulse-train phase shift needs to be shown. Instantaneous measurements of small phase shifts with a phase detector are usually difficult because of amplitude to phase conversion in the detector circuit. However, larger

constant shifts measured relative to the rf drive signal are straightforward. Figure 46.26 shows the effect of small changes in the laser cavity length on pulse-train phase shift using a differential micrometer. The data was taken over the course of about 10 min.

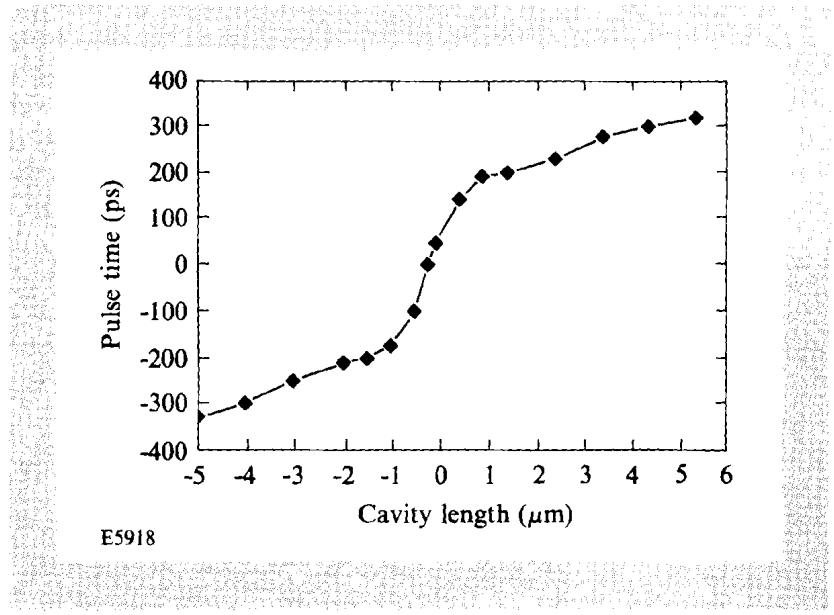

Fig. 46.26
The pulse-train phase is a strong function of laser cavity length. The region of steepest slope is where the mode-locked pulses are shortest. Outside of this region, the laser output power typically becomes less stable.

As is expected for a resonant system, the phase-shift slope is steepest where the cavity length results in a pulse round-trip frequency precisely equal to the rf drive frequency. The slope in this region is 130 ps/μm for a laser running with 80-ps pulses. Again, the results depend on details of the laser. If the laser is operated in the long-pulse regime, the slope in the resonance region is much smaller. For example, for a 750-ps-pulse laser the resulting phase (or timing) shift was found to be negligible over the same range of length adjustment.[3]

This data shows, therefore, that the phase of a short-pulse laser is sensitive to very small fluctuations in cavity length. Of course, this sensitivity is moderated at high frequency by the finite response time of the laser. The exact details of this issue are still under investigation.

Measurement of Cavity Fluctuations

Fluctuations in the laser cavity length due to component movements are easiest to eliminate. The mirrors must be carefully mounted, but this is a requirement of any mode-locked laser. A further consideration is that all

sources of vibration must be reduced as much as possible. Even coolant water flow can be a significant source of vibration for continuously pumped systems.

The source of a large fraction of cavity-length fluctuations in our test laser was the result of optical-path-length (OPL) changes in the gain medium. These seem to arise from vibrations induced by turbulent coolant flow over the rod. Measurements of OPL in the rod were made with a Mach-Zehnder interferometer around the laser head. The configuration is shown in Fig. 46.27. In order to include the effect of the vibrational source on the interferometer itself, two measurements were made with the coolant flowing in both cases. In case (a), the interferometer bypasses the rod to establish a baseline fluctuation due only to interferometer instability. In case (b), one arm is repositioned to include the Nd:YLF gain medium. The rod is not optically pumped. Figure 46.28 shows typical results for each case. We see that the OPL fluctuations in the rod are as much as 0.5 μm. This corresponds to a potential 60-ps shift in pulse-train timing or to a 38-mrad phase shift.

Stabilization Methods

Several active feedback techniques can be used to stabilize the phase of the output pulse train. One technique uses the phase of the laser output signal to control cavity length. A problem with this technique is that it adjusts cavity length for any phase change, even one from another source. Thus the cavity length can actually be detuned if the phase noise is a result of other sources.

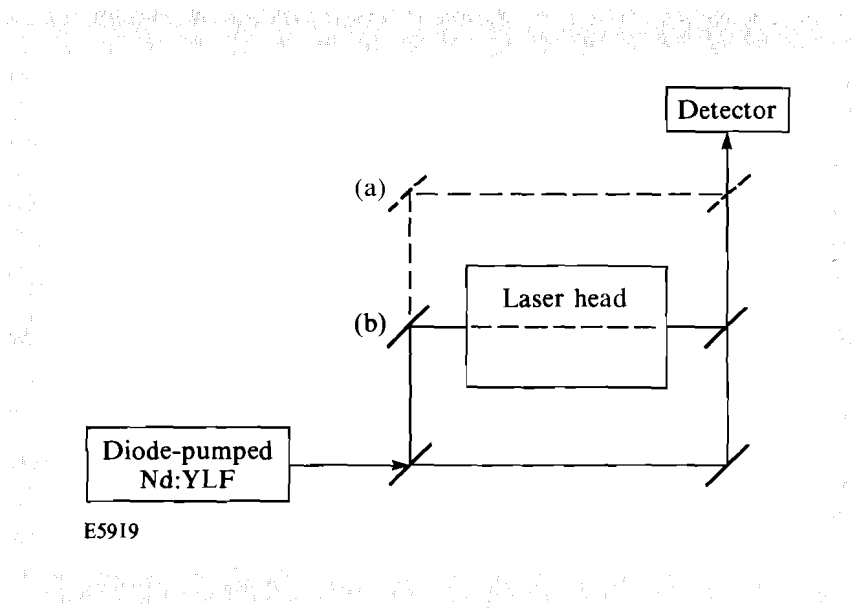

Fig. 46.27
A Mach-Zehnder interferometer where (a) the interferometer bypasses the laser rod, and (b) one arm passes through the 79-mm × 4-mm rod.

This could produce pulse-width broadening and even unstable laser operation.

In another technique one interferometrically compares and adjusts the laser longitudinal-mode frequencies to an external reference cavity. The advantage of this design is that it isolates cavity-length-induced phase changes from those of other sources, since the interferometer responds to the laser-frequency changes caused by small changes in oscillator OPL. The disadvantage is considerable added complexity and no direct measure of the laser output phase.

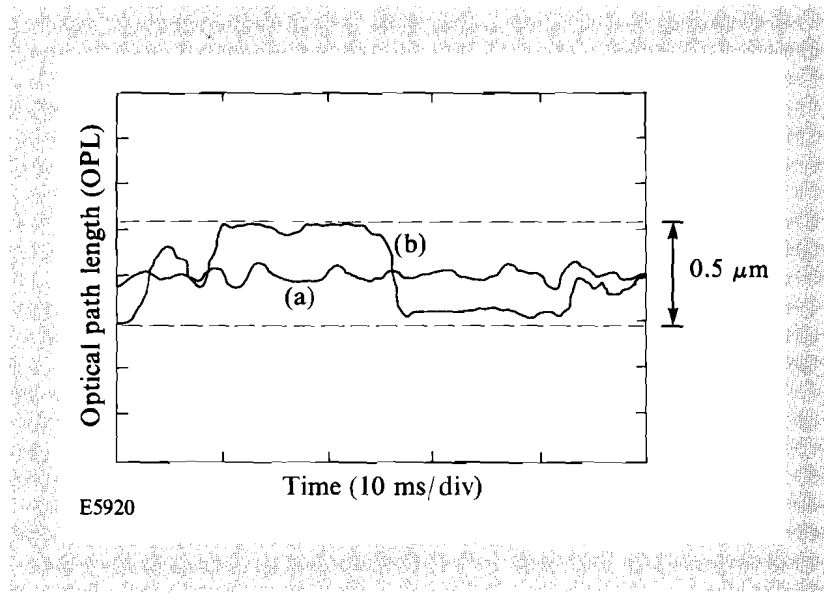

Fig. 46.28
The output from the interferometer shown in Fig. 46.27 where (a) the interferometer bypasses the laser rod, and (b) one arm passes through the rod. The optical-path-length (OPL) fluctuations are due to the turbulent water flow past the rod.

A third technique uses the output pulse-train phase to control the input rf phase to the mode locker.[2] While published results look encouraging, this method essentially works on the symptom of phase noise but does not attempt to correct its source (i.e., no adjustments are made directly to the laser parameters). For example, if the cavity length drifts slightly the laser pulse width may change, which could have an effect similar to a phase change on some experiments. The best solution might be a combination of the second and third techniques to achieve both long-term phase stability and improved overall long-term laser stability. The third technique measures phase directly so that it corrects for phase errors from any source while the second technique acts to maintain optimum cavity length, which is an important source of phase noise and laser instability.

Conclusion

We have found that both thermal and acoustic effects produce significant phase noise in short-pulse mode-locked lasers. We have also shown that severe constraints are placed on both laser cavity length and mode-locker temperature in order to achieve good phase stability of the laser-pulse train. Other effects may also contribute to pulse-train phase instabilities but further work is needed to identify them. By finding the sources of this noise, we hope to eliminate them or improve the effectiveness of active feedback techniques.

ACKNOWLEDGMENT

This work was supported by the U.S. Department of Energy Division of Inertial Fusion under agreement No. DE-FC03-85DP40200 and by the Laser Fusion Feasibility Project at the Laboratory for Laser Energetics, which has the following sponsors: Empire State Electric Energy Research Corporation, New York State Energy Research and Development Authority, Ontario Hydro, and the University of Rochester.

REFERENCES

1. D. von der Linde, *Appl. Phys. B* **39**, 201 (1986).
2. M. J. W. Rodwell *et al.*, *IEEE J. Quantum Electron.* **QE-25**, 817 (1989).
3. Unpublished LLE data.

Section 3
NATIONAL LASER USERS FACILITY NEWS

The proposals for FY92 NLUF projects were to be submitted to the DOE San Francisco office by 27 March 1991. The steering committee will meet during the first two weeks of May to review the technical merit of all proposals and will submit recommendations to DOE by 15 May 1991. DOE will reach its decision by 15 June 1991 and inform all principal investigators of the funding decisions. DOE funding for the accepted FY92 NLUF proposals is expected to be equal to that of FY91.

The University of Illinois conducted a series of AFOSR-funded experiments on the GDL laser system during the second quarter of FY91. These experiments were led by **G. Banas** and were done in collaboration with **H. E. Elsayed-Ali** of LLE's Ultrafast Sciences Group. The experiments were designed to study the material properties of metal weldments after they had been irradiated with a high-power laser beam. The irradiation was done with the GDL laser and the samples were taken back to the University of Illinois for characterization.

J. Moreno from **H. Griem's** group at the University of Maryland took some time-dependent XUV spectral data on LLE implosion targets. These shots were part of an experiment that will study the spectral emission from both the radiation heat front as well as the imploded core. These were the first of the targets slated for FY91 and served as a check of the diagnostic.

Section 4
LASER SYSTEM REPORT

4.A GDL Facility Report

During the second quarter of FY91, the regenerative amplifier pulse-shaping system was removed from GDL and GDL was realigned in preparation for NLUF experiments. At the end of the quarter, users from the University of Illinois began a series of experiments on laser annealing.

The shot summary for the GDL laser this quarter is as follows:

Laser system		24
Calibration		16
Users		51
	TOTAL	91

ACKNOWLEDGMENT

This work was supported by the U.S. Department of Energy Division of Inertial Fusion under agreement No. DE-FC03-85DP40200 and by the Laser Fusion Feasibility Project at the Laboratory for Laser Energetics, which has the following sponsors: Empire State Electric Energy Research Corporation, New York State Energy Research and Development Authority, Ontario Hydro, and the University of Rochester.

4.B OMEGA Facility Report

The OMEGA Laser Facility was scheduled for several target campaigns during the second quarter of FY91. However, because of problems in several areas of the system, only one campaign was completed and another was begun.

Problem areas included the power-conditioning system, the alignment computer, and the driver line. After total failure of the old FORTH-based alignment system, sufficient portions of the new limited-alignment system were introduced on a "crash" basis so as to enable limited-alignment operation. The driver line was completely realigned and a number of mounts suspected of causing drift were replaced.

The completed campaign was a series of burnthrough targets used to study implosion stability. At the end of the quarter a series of long-scale-length plasma experiments were started on flat targets.

The shot summary for OMEGA this quarter is as follows:

Laser test		260
Target		87
	TOTAL	347

ACKNOWLEDGMENT

This work was supported by the U.S. Department of Energy Division of Inertial Fusion under agreement No. DE-FC03-85DP40200 and by the Laser Fusion Feasibility Project at the Laboratory for Laser Energetics, which has the following sponsors: Empire State Electric Energy Research Corporation, New York State Energy Research and Development Authority, Ontario Hydro, and the University of Rochester.

PUBLICATIONS AND CONFERENCE PRESENTATIONS

Publications

S. H. Batha, D. D. Meyerhofer, A. Simon, and R. P. Drake, "Raman Up-Scattering in Long-Scale-Length, Laser-Produced Plasmas," *Phys. Fluids B* **3**, 448–454 (1991).

T. Boehly, M. Russotto, R. S. Craxton, R. Epstein, B. Yaakobi, L. B. DaSilva, J. Nilsen, E. A. Chandler, D. J. Fields, B. J. MacGowan, D. L. Matthews, J. H. Scofield, and G. Shimkaveg, "Demonstration of a Narrow Divergence X-Ray Laser in Neon-Like Titanium," *Phys. Rev. A* **42**, 6962–6965 (1990).

H. C. Chen, G. A. Mourou, and R. Knox, "Subnanosecond Time-Resolved Electron Diffraction from Thin Crystalline Gold Films," *Beam-Solid Interactions: Physical Phenomena* (MRS, Pittsburgh, PA, 1990), Vol. 157, pp. 437–442.

P. C. Cheng, V. H.-K. Chen, H. G. Kim, and R. E. Pearson, "An EPI-Fluorescent Spinning-Disk Confocal Microscope," in the *Proceedings of the 47th Annual Meeting of Electron Microscopy Society of America* (EMSA), San Antonio, TX, 14–18 August 1989, pp. 136–137.

Y.-H. Chuang, Z.-W. Li, D. D. Meyerhofer, and A. Schmid, "Nonresonant $\chi^{(3)}_{1111}$ Obtained by Nearly-Degenerate Four-Wave Mixing Using Chirped-Pulse Technology," *Opt. Lett.* **16**, 7–9 (1991).

J. A. Delettrez and E. M. Epperlein, "Comments on 'Modified Nonlocal Heat-Transport Formula for Steep Temperature Gradients'," *Phys. Rev. A* **43**, 3174–3175 (1991).

H. E. Elsayed-Ali, T. Juhasz, G. O. Smith, and W. E. Bron, "Femtosecond Thermoreflectivity and Thermotransmissivity of Polycrystalline and Single-Crystalline Gold Films," *Phys. Rev. B* **43**, 4488–4491 (1991).

R. Epstein, "Satellite Absorption Lines and the Temperature Dependence of X-Ray Absorption Features in High-Temperature Plasmas," *Phys. Rev. A* **43**, 961–967 (1991).

S. D. Jacobs, "Building Blocks for Better Lasers," *Chemtech*, 106–115 (1991).

J. C. Lee, S. D. Jacobs, and K. J. Skerrett, "Laser Beam Apodizer Utilizing Gradient-Index Optical Effects in Liquid Crystals," *Opt. Eng.* **30**, 330–336 (1991).

S. Papernov, K. Marshall, M. Guardalben, A. Schmid, and S. D. Jacobs, "351 nm, 0.7-ns Laser Damage Thresholds of Monomeric Liquid-Crystalline Systems," *Liq. Cryst.* **9**, 71–76 (1991).

C. Pruitt, "A Generalized EXIT," *J. Forth Appl. & Res.* **6**, 157–164 (1991).

M. D. Skeldon and R. E. Bahr, "Stimulated Rotational Raman Scattering in Air with a High-Power Broadband Laser," *Opt. Lett.* **16**, 366–368 (1991).

Forthcoming Publications

S. Alexandrou, R. Sobolewski, H. Nakano, B. C. Tousley, and T. Y. Hsiang, "Picosecond Characterization of Bent Coplanar Waveguides," to be published in *IEEE Microwave and Guided Wave Letters*.

H. Chen, Y.-H. Chuang, J. A. Delettrez, S. Uchida, and D. D. Meyerhofer, "Study of X-Ray Emission from Picosecond Laser-Plasma Interaction," to be published in the *Proceedings of the SPIE's OE/LASE '91 Symposium*, Los Angeles, CA, 20–25 January 1991.

P.-C. Cheng, H. Kim, and T. H. Lin, "The Study of Silica Deposition in the Leaf Blade of Zea mays L. by X-Ray Contact Microradiography and Confocal Microscopy," to be published in *X-Ray Microscopy III*, edited by A. Michette *et al.* (Springer-Verlag, New York).

Y.-H. Chuang, D. D. Meyerhofer, S. Augst, H. Chen, J. Peatross, and S. Uchida, "Suppression of the Pedestal in a Chirped-Pulse-Amplification Laser," to be published in the *Journal of the Optical Society of America B (Optical Physics)*.

Y.-H. Chuang, J. Peatross, and D. D. Meyerhofer, "Modeling the Pedestal in a Chirped-Pulse-Amplification Laser," to be published in the *Proceedings of the SPIE's OE/LASE'91 Symposium*, Los Angeles, CA, 20–25 January 1991.

J. Delettrez, R. Epstein, D. K. Bradley, P. A. Jaanimagi, R. C. Mancini, and C. F. Hooper, "Hydrodynamic Simulations, with Non-LTE Atomic Physics, of High-Density Implosions of Argon-Filled Polymer Shell Targets," to be published in the *Proceedings of the 1990 International Workshop on Radiative Properties of Hot Dense Matter*, Sarasota, FL, 22–26 October 1990.

H. E. Elsayed-Ali, J. W. Herman, and K. K. Lo, "Picosecond Time-Resolved Electron Diffraction Studies of Laser Heated Metals," to be published in the *Proceedings of the International Conference on Lasers '90*, STS Press, McLean, VA, 10–14 December 1990 (invited paper).

E. M. Epperlein, "Electron Kinetics in Laser-Driven Inertial Confinement Fusion," to be published in the *Proceedings of the Topical Conference on Research Trends in Nonlinear and Relativistic Effects in Plasmas*, La Jolla, CA, 5–8 February 1990.

R. Epstein and B. Yaakobi, "The Effect of Photoelectric Fluorescence on the Formation of X-Ray Absorption Lines in Laser-Plasma Experiments," to be published in *Physical Review A*.

P. M. Fauchet, "Applied Optical Diagnostics of Semiconductors," to be published in *IEEE Journal of Quantum Electronics* (invited paper).

P. M. Fauchet, D. A. Young, W. L. Nighan, Jr., and C. M. Fortmann, "Picosecond Carrier Dynamics in a-$Si_{0.5}Ge_{0.5}$:H Measured with a Free Electron Laser," to be published in *IEEE Journal of Quantum Electronics*.

D. Golini and S. D. Jacobs, "The Physics of Loose Abrasive Microgrinding," to be published in *Applied Optics*.

T. Gong and P. M. Fauchet, "Femtosecond Refractive and Absorptive Nonlinearities Due to Real Carriers in GaAs," to be published in the *Proceedings of the IEEE/Lasers and Electro-Optics Society of America, Picosecond Electronics and Optoelectronics Conference*, Salt Lake City, UT, 13–15 March 1991.

T. Gong, P. Mertz, W. L. Nighan, Jr., and P. M. Fauchet, "Femtosecond Carrier Induced Changes of Refractive Index in GaAs," to be published in *Applied Physics*.

A. Honig, N. Alexander, Q. Fan, R. Q. Gram, and H. Kim, "Absence of Molecular Deuterium Dissociation During Room-Temperature Permeation into Polystyrene ICF Target Shells," to be published in the *Journal of Vacuum Science and Technology A*.

J. H. Kelly, M. Shoup III, M. D. Skeldon, and S. T. Bui, "Design and Energy Characterization of a Multi-Segment Glass Disk Amplifier," to be published in the *Proceedings of the SPIE's OE/LASE '91 Symposium*, Los Angeles, CA, 20–25 January 1991.

H. Kim, B. Yaakobi, J. M. Soures, and P.-C. Cheng, "Laser-Produced Plasma as a Source for X-Ray Microscopy," to be published in *X-Ray Microscopy III*, edited by A. Michette *et al.* (Springer-Verlag, New York).

H. G. Kim, C. K. Immesoete, and S. Scarantino, "Computer-Assisted Microballoon Selection for Inertial Fusion Targets," to be published in the *Proceedings of the Seventh Target Fabrication Specialists Meeting*, Livermore, CA, 25–29 September 1989.

H. G. Kim, R. Q. Gram, M. D. Wittman, C. Immesoete, R. S. Craxton, N. Sampat, S. Swales, G. Pien, and J. M. Soures, "Uniform Liquid Fuel Layer

Produced in a Cryogenic Target by a Time-Dependent Thermal Gradient," to be published in the *Proceedings of the Seventh Target Fabrication Specialists Meeting*, Livermore, CA, 25–29 September 1989.

S. Krishnamurthy and S. H. Chen, "New Thermotropic Chiral Nematic Copolymers. II. A Study of Helical Sense and Twisting Power Based on Copolymers Containing (S)-(-)-1-Phenylethyl Alcohol and (R)-(-)-Methyl Mandelate," to be published in *Macromolecules.*

S. Krishnamurthy and S. H. Chen, "Facilitating the Grandjean Texture Formation in Thermotropic Chiral Nematic Side-Chain Copolymers via Modulation of Backbone Flexibility," to be published in *Macromolecules.*

J. C. Lambropoulos and S.-S. Hwang, "Film Thermal Conductivity and Laser Damage Resistance of Optical Thin Films," to be published in the *Proceedings of a Symposium on Electro-Optics and Non-Linear Optics, 1st International Congress on Ceramic Science and Technology*, Anaheim, CA, 1–3 November 1989.

Y. Lin, W. D. Seka, J. H. Eberly, H. Huang, and D. L. Brown, "Experimental Investigation of Bessel Beam Characteristics," to be published in *Applied Optics (Lasers and Photonics).*

G. G. Luther, C. J. McKinstrie, and A. L. Gaeta, "The Transverse Modulational Instability of Counterpropagating Light Waves," to be published in the *Proceedings of the Topical Meeting on Nonlinear Dynamics in Optical Systems*, Afton, OK, 4–8 June 1990.

R. L. McCrory, "Laser-Driven ICF Experiments," to be published in *Nuclear Fusion by Inertial Confinement*, edited by G. Velerade, Y. Ronen, and J. M. Martinez-Val (CRC Press).

R. L. McCrory and C. P. Verdon, "Computer Modeling and Simulation in Inertial Confinement Fusion," to be published in *Il Nuovo Cimento.*

R. L. McCrory and C. P. Verdon, "Inertial Confinement Fusion: Computer Simulation," to be published in *Computer Applications of Plasma Science and Engineering*, edited by A. Drobot (Springer Verlag, New York).

R. L. McCrory, J. M. Soures, J. Knauer, S. Letzring, F. J. Marshall, S. Skupsky, W. Seka, C. Verdon, D. Bradley, R. S. Craxton, J. Delettrez, R. Epstein, P. Jaanimagi, R. Keck, T. Kessler, H. Kim, R. Kremens, P. W. McKenty, R. Short, and B. Yaakobi, "Direct-Drive Implosion Experiments at the Laboratory for Laser Energetics," to be published in the *Proceedings of the Thirteenth International Conference on Plasma Physics and Controlled Nuclear Fusion Research*, Washington, DC, 1–6 October 1990.

R. L. McCrory, J. M. Soures, J. P. Knauer, S. A. Letzring, F. J. Marshall, S. Skupsky, W. D. Seka, C. P. Verdon, D. K. Bradley, R. S. Craxton, J. A. Delettrez, R. Epstein, P. A. Jaanimagi, R. L. Keck, T. J. Kessler, H. Kim, R. L. Kremens, P. W. McKenty, R. W. Short, and B. Yaakobi, "Short-Wavelength-Laser Requirements for Direct-Drive Ignition and Gain," to be published in the *Proceedings of the International Atomic Energy Agency*

(IAEA) Topical Committee Meeting on Drivers for Inertial Confinement Fusion, Osaka, Japan, 15–19 April 1991.

C. J. McKinstrie and M. Yu, "The Role of Ion Momentum in Stimulated Raman Scattering," to be published in *Physics of Fluids B*.

C. J. McKinstrie and R. Bingham, "Stimulated Raman Forward Scattering and the Relativistic Modulational Instability of Light Waves in Rarefied Plasma," to be published in *Physics of Fluids B*.

E. A. Murphy, H. E. Elsayed-Ali, K. T. Park, J. Cao, and Y. Gao, "Angle Resolved X-Ray Photoemission Study of the Surface Disordering of Pb(100)," to be published in *Physical Review B*.

D. Y. Park, W. Seka, Y. Lin, and D. L. Brown, "Operational Characteristics of an Imaging, Unstable Ring Resonator Using Nd:YLF as Active Medium," to be published in the *Proceedings of the Ninth Workshop on Laser Interaction and Related Plasma Phenomena*, Monterey, CA, 6–10 November 1989.

J. K. Samarabandu, R. Acharya, C. D. Edirisinghe, P. C. Cheng, H. Kim, T. H. Lin, R. G. Summers, and C. E. Musial, "Analysis of Multi-Dimensional Confocal Images," to be published in the *Proceedings of the SPIE Symposium "Biomedical Imaging,"* San Diego, CA, 24 February 1991.

N. Sampat, "RS-170 Video Standard + Scientific Imaging = Plenty of Headaches," to be published in *Advanced Imaging*.

W. Seka, D. Golding, B. Klein, R. J. Lanzafame, and D. Rogers, "Laser Energy Repartition Inside Metal, Sapphire, and Quartz Surgical Laser Tips," to be published in the *Proceedings of SPIE's Application of Optical Engineering CAN-AM Eastern '90 on Optical Engineering*, Rochester, NY, 4–5 October 1990.

W. D. Seka, R. S. Craxton, R. E. Bahr, D. L. Brown, D. K. Bradley, P. A. Jaanimagi, B. Yaakobi, and R. Epstein, "Production and Characterization of Hot, Long-Scale-Length Laser Plasmas," to be published in *Physics of Fluids*.

L. J. Shaw-Klein, S. J. Burns, and S. D. Jacobs, "Thermal Conductivity of Aluminum Nitride Thin Films," to be published in *MRS Symposium Proceedings Series—Electronic Packaging Materials Science*.

Conference Presentations

The following presentations were made at the SPIE's OE/LASE '91 Symposium, Los Angeles, CA, 20–25 January 1991:

D. L. Brown, W. Seka, and S. A. Letzring, "Toward Phase Noise Reduction in a Nd:YLF Laser Using Electro-Optic Feedback Control."

Y.-H. Chuang, D. D. Meyerhofer, S. Augst, H. Chen, J. Peatross, and S. Uchida, "Suppression of the Pedestal in a Chirped-Pulse-Amplification Laser."

Y.-H. Chuang, J. Peatross, and D. D. Meyerhofer, "Modeling the Pedestal in a Chirped-Pulse-Amplification Laser."

J. H. Kelly, M. Shoup III, M. D. Skeldon, and S. T. Bui, "Design and Energy Characterization of a Multi-Segment Glass Disk Amplifier."

T. J. Kessler, T. R. Boehly, R. S. Craxton, J. H. Kelly, C. D. Kiikka, S. A. Kumpan, S. Skupsky, J. M. Soures, and C. Verdon, "OMEGA Laser Upgrade for Direct Drive Inertial Confinement Fusion."

M. D. Skeldon, M. S. Jin, D. J. Smith, and S. T. Bui, "Performance of a Longitudinal Mode KDP Pockels Cell with Transparent Conductive Coatings."

J. P. Chu, G. Banas, H. E. Elsayed-Ali, J. M. Rigsbee, and F. V. Lawrence, "Laser-Shock Hardening of Iron-Based Materials," presented at the 1991 TMS Annual Meeting, New Orleans, LA, 17–21 February 1991.

H. Kim, "Applications of Laser-Produced Plasma as an X-Ray Source," presented at the 1991 Wave and Laser Symposium, Optical Society of Korea, Daeduk, Korea, 20 February 1991 (invited talk).

The following presentations were made at the IEEE/Lasers and Electro-Optics Society of America, Picosecond Electronics and Optoelectronics Conference, Salt Lake City, UT, 13–15 March 1991:

T. Gong and P. M. Fauchet, "Femtosecond Refractive and Absorptive Nonlinearities Due to Real Carriers in GaAs."

T. Gong, P. Mertz, and P. M. Fauchet, "Femtosecond Refractive Nonlinearities Due to Real Carriers in GaAs."

The following presentations were made at the American Physical Society Meeting, Cincinnati, OH, 18–22 March 1991:

T. Juhasz, X. H. Hu, W. E. Bron, and H. E. Elsayed-Ali, "Temperature Dependence of Time-Resolved Thermoreflectivity of Single Crystalline Gold Thin Films."

E. A. Murphy, H. E. Elsayed-Ali, K. T. Park, J. Cao, and Y. Gao, "Angle Resolved X-Ray Photoemission Study of the Surface Disordering of Pb(100)."

ACKNOWLEDGMENT

The work described in this volume includes current research at the Laboratory for Laser Energetics, which is supported by Empire State Electric Energy Research Corporation, New York State Energy Research and Development Authority, Ontario Hydro, the University of Rochester, and the U.S. Department of Energy Division of Inertial Fusion under agreement No. DE-FC03-85DP40200.

UNIVERSITY OF
ROCHESTER